

# Self-Consistent Modelling of Neutrino Production in Turbulent Black Hole Coronae

S. Le Bihan<sup>1</sup>, M. Lemoine<sup>1</sup>, and F. Rieger<sup>2,3</sup>

<sup>1</sup> Université Paris Cité, CNRS, Astroparticule et Cosmologie, F-75013 Paris, France  
e-mail: lebian@apc.in2p3.fr  
e-mail: mlemoine@apc.in2p3.fr

<sup>2</sup> Max Planck Institute for Plasma Physics (IPP), Boltzmannstraße 2, 85748 Garching, Germany

<sup>3</sup> Institute for Theoretical Physics, Heidelberg University, Philosophenweg 12, 69120 Heidelberg, Germany  
e-mail: frank.rieger@ipp.mpg.de

Received XX XX, 20XX

## ABSTRACT

Stochastic particle acceleration in magnetized turbulent plasmas has emerged as a key mechanism to explain multi-messenger signals from compact astrophysical environments. Self-consistent modelling remains challenging because it requires to treat simultaneously several non-linear kinetic processes, especially turbulence-driven acceleration and its feedback on the turbulent cascade, as well as the radiative and hadronic losses, including the reprocessing of electromagnetic radiation in radiatively dense environments. The present paper introduces the hybrid numerical code *Turb-AM3* designed to this effect. This hybrid numerical code couples the state-of-the-art time-dependent lepto-hadronic radiative solver *AM3* with a stochastic acceleration module that incorporates recent theoretical advances in turbulent acceleration and accounts for the dynamical damping of turbulence by accelerated particles. In a second part, we use this code to provide self-consistent time-dependent models of proton acceleration in the turbulent black hole corona of NGC 1068. We find that the IceCube neutrino signal is well reproduced for a standard set of physical parameters describing the black hole corona. The same template model accounts in a satisfactory way for IceCube observations of other active galactic nuclei. Furthermore, our exploration of parameter space allows us to predict detailed template spectral shapes for the TeV neutrino spectrum, which in turn help understand how future neutrino observations can constrain the properties of turbulent AGN coronae and the underlying acceleration mechanism. This *Turb-AM3* framework provides a powerful tool to model multi-messenger emission in a broad variety of compact astrophysical environments.

**Key words.** Galaxies: active – Acceleration of particles – Black hole physics – Neutrinos – Turbulence

## 1. Introduction

In 2022, the IceCube Collaboration reported a  $4.2\sigma$  statistical excess of high-energy neutrinos in the  $\sim 1$ -10 TeV range spatially associated with the nearby Seyfert 2 galaxy NGC 1068 (Aartsen et al. 2020; IceCube Collaboration et al. 2022), which, if confirmed, represents a dramatic step forward in our exploration of the high-energy multi-messenger sky. While this active galactic nucleus (AGN) provides today the most compelling source of high-energy neutrinos, statistical evidence for correlation with other nearby Seyfert galaxies (e.g., NGC 4151, NGC 7469,  $\sim 3.0\sigma$  for both and at  $E_\nu \simeq 5$ –50 TeV and  $E_\nu \simeq 50$ –100 TeV respectively, Abbasi et al. 2026) has been building up in recent years (Abbasi et al. 2025a,b), suggesting that non-jetted AGN environments are significant contributors to the extragalactic neutrino flux (Padovani et al. 2024; Neronov et al. 2024; Fiorillo et al. 2025; Murase et al. 2026; Yang et al. 2026). These results expand the landscape of possible sources beyond the flaring blazar TXS 0506+056 (IceCube Collaboration et al. 2018; IceCube et al. 2018), other jetted candidates like PKS 1424-240 and GB6 J1542+61 (IceCube Collaboration et al. 2022), and tidal disruption events (Stein et al. 2021; Reusch et al. 2022; Lu et al. 2025).

NGC 1068 is a long-studied source due to its relative proximity of  $\simeq 10$  Mpc (Tully et al. 2009; Lianou et al. 2019). Low-frequency observations of its nucleus point to

heavy obscuration below the MeV range by a dense dusty torus, that absorbs the primary radiation from the accretion disk and corona and re-emits it in the infrared band (e.g. Jaffe et al. 2004). As a consequence, the intrinsic emission from the innermost regions of the AGN cannot be directly probed at X-ray energies. In the  $\gamma$ -ray domain, observations with *Fermi*-LAT and MAGIC (The Fermi Collaboration 2020; MAGIC Collaboration et al. 2019) place stringent upper limits on the  $\gamma$ -ray flux, at least an order of magnitude below the neutrino flux inferred by IceCube. This striking mismatch between the neutrino and  $\gamma$ -ray emissions is widely interpreted as evidence that neutrinos are produced in a compact region that is opaque to high-energy photons, due to efficient  $\gamma\gamma$  absorption in an intense radiation field (Inoue et al. 2019; Murase et al. 2020; Kheirandish et al. 2021; Murase 2022; Eichmann et al. 2022; Ajello et al. 2023; Fang et al. 2023; Padovani et al. 2024; Murase et al. 2024; Das et al. 2024). While alternative explanations have been proposed (e.g., Herrera 2025), the most compelling interpretation points toward a dense, compact emission zone, most plausibly the turbulent AGN corona of the supermassive black hole (BH). The observed multi-messenger signals from NGC 1068 therefore provide a unique indirect probe of particle acceleration to very high energies and radiative processes in the immediate environment of black holes.

In this emerging context, proton acceleration to  $\sim 10 - 100$  TeV in AGN cores has received increased attention in recent years, whether around accretion shock waves, in magnetic reconnection layers, in the magnetized turbulence, in shear layers at the jet base, or a combination of these processes, see the above references as well as, e.g., Fiorillo et al. (2024b); Mbarek et al. (2024); Lemoine & Rieger (2025); Ambrosone (2024); Yang et al. (2025); Yuan et al. (2026); Karavola et al. (2025); Nhat Ly et al. (2026); Testagrossa et al. (2026). As AGN coronae are generically regarded as magnetically-dominated, highly turbulent environments, stochastic acceleration in the magnetized turbulence emerges as a natural and promising mechanism, and we focus on this scenario in the present paper.

Theoretical models of AGN coronae have traditionally focused on the energization processes of leptons (electrons and positrons) and their radiative processes, notably inverse Compton scattering and pair production, shaping the X-ray spectra of the AGN (e.g., Fabian et al. 2015, 2017; Beloborodov 2017; Kammoun et al. 2024, for a few recent references). The high compactness of AGN coronae implies that electrons cool on short timescales  $\ll R_{\text{cor}}/c$ , where  $R_{\text{cor}} \sim \mathcal{O}(10 r_g)$  denotes the corona size and  $r_g$  the gravitational radius, assuming cooling to be inverse Compton dominated.

Consequently, the electron distribution remain mostly thermal at temperatures  $k_B T_e \sim \mathcal{O}(100 \text{ keV})$ , albeit with possibly a small non-thermal fraction. The numerical simulation of the underlying microphysical processes has recently become accessible to particle-in-cell (PIC) codes incorporating radiative processes (Groselj et al. 2024; Nätilä 2024; Groselj et al. 2026). These simulations provide conclusive evidence that a strongly turbulent corona with characteristic Alfvén velocity  $v_A \gtrsim 0.1 c$  and compactness in the expected range can reproduce the generic X-ray power law-like spectra, providing further support to the idea that these magnetized turbulent environments can also accelerate protons efficiently. However, contrary to the electron population, the proton distribution evolves on macroscopic timescales of the order of  $R_{\text{cor}}/v_{\text{adv}}$ , where  $v_{\text{adv}} \lesssim 0.1 c$  denotes the flow velocity in the corona. Furthermore, simulating the acceleration of protons up to the energies inferred by IceCube would require a dynamical range covering at least 5 orders in magnitude. This problem is thus bound to remain out of reach of PIC simulations, at least for a long time.

The most promising, as well as standard, way to bridge this gap in scales is to track the evolution of particle distribution functions through macroscopic transport equations integrating models benchmarked on kinetic simulations as well as constraints on the ambient physical conditions derived from observations or general-relativistic magnetohydrodynamic (GRMHD) simulations. Steps in this direction have been taken in the aforementioned references, although often at the price of diverse approximations, e.g., using semi-analytical accelerated proton spectra and/or radiative losses, a steady state description, modelling acceleration with prescribed radiative losses, etc. The problem indeed shares similar degrees of complexity with models of coronal X-ray emission, as it requires a time-dependent treatment of acceleration and of radiative losses, including the reprocessing of electromagnetic radiation. To address these issues, we introduce here a novel hybrid numerical framework, Turb-AM3, specifically designed to model stochastic particle acceleration in compact environments and to predict the ensuing multi-messenger signatures in a self-consistent manner. The code couples the time-dependent lepto-hadronic radiative solver AM3 (Klinger et al. 2024) with a stochastic-acceleration module, which offers a detailed treatment of charged-particle

energization in turbulent plasmas. Particle acceleration is described through a momentum-space transport equation that incorporates recent theoretical developments, while the framework self-consistently evolves the magnetic turbulent cascade and includes a physically motivated description of the environment, including radiative (soft photon) field and plasma flow. The AM3 module computes all relevant radiative and hadronic losses and tracks the production and propagation of secondary particles, including photons and neutrinos, carefully accounting for the development of electromagnetic cascade. This numerical framework is similar in spirit to that recently proposed in Yuan et al. (2026), but contains additional features of interest that we discuss in forthcoming sections. This includes, in particular, a self-consistent description of the feedback exerted by accelerated particles on the magnetized turbulence, and hence on the acceleration process, which is potentially significant in the present context given the inferred (high) proton luminosities. The code architecture and main principles are discussed in Sect. 2.

We then use Turb-AM3 to investigate the specific case of stochastic acceleration in the turbulent BH corona of NGC 1068 and to derive self-consistent proton, photon, and neutrino spectra. Template neutrino spectra are of particular importance to both enhance the sensitivity of neutrino telescopes searches and to constrain the overall contribution of BH coronae to the diffuse neutrino background. As we discuss in the forthcoming sections, our investigation also offers new insights on key open issues, such as the main physical parameters governing the neutrino spectral shape and luminosity, the effects of non-linear proton acceleration and radiation (e.g., impact on coronal turbulence and hadronic-induced pair production), and the expected characteristics of the lower-energy ( $E \sim 1-100$  GeV) neutrino signal. Our model is self-consistent in that it treats simultaneously the non-linear and time-dependent aspects of proton acceleration and neutrino production, bridging the gap between PIC simulation scales and those of the source. In this mindset, we borrow insights from recent PIC simulations to inform and improve our analysis. While the corona is modeled as a one-zone system in this study, the framework can be extended to state-of-the-art, position-dependent physical parameters as could be derived from, e.g. radiative GRMHD simulations. It is of broad applicability, and in the spirit of AM3 (Klinger et al. 2024) and similar codes (e.g., Cerruti et al. 2026, and references therein), it could also be applied to other sources, such as hidden-neutrino sources, AGN jets (Rodrigues et al. 2024), X-ray binaries (Kantzas et al. 2023), and/or tidal disruption events (Yuan et al. 2024) with suitable adjustments.

This paper is organized as follows. We present the physical framework of the model in Sect. 2, starting with a generic description of the AGN corona, followed by the particle acceleration mechanism, the evolution of the turbulent cascade, and the numerical implementation of Turb-AM3. In Sect. 3, we apply our study to the case of NGC 1068 and discuss the multi-messenger signatures. We investigate the dependence on the (broad) parameter space in Sect. 3.2, and extract template neutrino spectra for turbulent acceleration. In Sect. 3.4, we further show that the model provides a satisfactory match to the multi-messenger data of other Seyfert galaxies identified by IceCube (NGC 4151 and NGC 7469). We summarize our findings in Sect. 4. Throughout this work, we use  $Q_x/Q = 10^x$  in cgs units unless otherwise noted.

## 2. Physical and numerical set-up

In this section, we present the physical assumptions and numerical framework used to model particle acceleration, transport, and radiation in AGN coronae.

### 2.1. Corona model

We consider a general AGN configuration in which a supermassive black hole (SMBH) of mass  $M_{\text{BH}}$ , with gravitational radius  $r_g \equiv GM_{\text{BH}}/c^2$ , is surrounded by an accretion disk of luminosity  $L_d$ . In the case of NGC 1068,  $M_{\text{BH}} \approx 10^{7.2} M_\odot$  and  $L_d \approx 5.0 \times 10^{44} \text{ erg s}^{-1}$  (Woo & Urry 2002; Lopez-Rodriguez et al. 2018). Above and below the disk, a hot, magnetized plasma forms a compact corona. Throughout this work the corona is assumed to be approximately spherical, with a characteristic size  $R_{\text{cor}} \lesssim 30 r_g$ , consistent with constraints for NGC 1068, especially the opacity needed for  $\gamma\gamma$  absorption to be efficient (Das et al. 2024). This approximation remains reasonable for the present purposes, as what truly matters is the effective size  $R_{\text{cor}}$ , which controls the losses through diffusive escape, the overall radiative opacity and the energy density of radiative backgrounds.

The corona is moderately thick to Thomson scattering, with optical depth  $\tau_T = n_e R_{\text{cor}} \sigma_T \lesssim 1$  (Zdziarski 1985; Stern et al. 1995; Ricci et al. 2018), in terms of  $n_e$  the total electron and positron number density, including pairs produced in situ. The pair content of AGN coronae is not currently well constrained on observational grounds (Fabian et al. 2015; Ricci et al. 2018; Hinkle & Mushotzky 2021). The pair loading factor, expressed as the ratio of proton to electron plus positron number densities,  $n_p/n_e$ , is regulated by the balance between photon-photon pair production and pair annihilation, and hence depends on the photon and electron energy distributions (e.g., Zdziarski & Lightman 1985; Poutanen & Svensson 1996; Fabian et al. 2017). It can therefore be obtained only through detailed modelling of X-ray data, at the price of assumptions regarding the microphysics of electron energization and of the photon backgrounds. In this work, we adopt a fiducial pair-free configuration,  $n_p/n_e = 1$ , but discuss its influence on the parameters further below as well as in Sect. 3.2; see also Yang et al. (2025). Numerically, the electron number density is given by

$$n_e \approx 2 \times 10^{10} \text{ cm}^{-3} \frac{\tau_T}{0.5} \frac{R_{\text{cor}}}{15 r_g} M_{7.2}. \quad (1)$$

The corona is assumed to be predominantly powered by the dissipation of magnetic energy, e.g. Galeev et al. (1979). As the dissipated energy of the turbulence is converted into the X-ray spectrum on short timescales due to the high compactness (Beloborodov 2017; Groselj et al. 2024, 2026), the steady state energy density of X-ray radiation can be expressed as

$$u_X \approx \frac{t_{\gamma,\text{esc}}}{t_{\text{diss}}} \frac{\delta B^2}{8\pi} \quad (2)$$

where  $t_{\gamma,\text{esc}} \approx (1 + \tau_T)R_{\text{cor}}/c$  represents the characteristic escape timescales of photons, and  $t_{\text{diss}} \approx f_{\text{diss}} \ell_c / v_A$  a typical time for dissipation of magnetic turbulence, with  $\ell_c$  the coherence length of the turbulence. The velocity  $v_A = \delta B / \sqrt{4\pi n_p m_p}$  is here understood as the Alfvénic velocity of magnetic fluctuations, which sets the characteristic velocity of the turbulent motions. We further assume  $f_{\text{diss}} = 0.1$ , as dissipation takes several turn-around times to proceed; this value also corresponds to the reconnection rate, which provides the relevant scaling in relativistic turbulence (Fiorillo et al. 2024a). Noting that the X-ray luminosity

$L_X = V_{\text{cor}} u_X / t_{\gamma,\text{esc}}$  where  $V_{\text{cor}}$  denotes the volume of the corona, and using Eqs. (1) together with (2), we obtain

$$\begin{aligned} \delta B &\approx 4.8 \times 10^3 \text{ G} L_{X44}^{1/3} \left( \frac{R_{\text{cor}}}{15 r_g} \right)^{-7/6} \left( \frac{\ell_c}{5 r_g} \right)^{1/3} M_{7.2}^{-5/6}, \\ v_A &\approx 0.2c L_{X44}^{1/3} \left( \frac{R_{\text{cor}}}{15 r_g} \right)^{-2/3} \left( \frac{\ell_c}{5 r_g} \right)^{1/3} M_{7.2}^{-1/3}, \end{aligned} \quad (3)$$

with  $M_{7.2} \equiv M_{\text{BH}}/10^{7.2} M_\odot$ ,  $L_{X44} \equiv L_X/10^{44} \text{ erg/s}$ . The numerical estimates for  $B$  and  $v_A$  assume  $n_p/n_e = 1$  and  $f_{\text{diss}} = 0.1$ ; they scale as  $f_{\text{diss}}^{-1/3} (n_p/n_e)^{1/6}$  and  $f_{\text{diss}}^{-1/3} (n_p/n_e)^{-1/3}$  respectively. The corresponding plasma  $\beta_p \equiv P_{\text{th}}/(\delta B^2/8\pi)$  parameter is of the order of unity for a proton temperature  $T_p \sim 2 \times 10^{11} \text{ K}$  (close to the virial temperature at  $R_{\text{cor}} = 15 r_g$ ). Following Gorbunov et al. (2025), we note that  $\beta_p \sim 1$  follows from the balance between turbulent dissipation and particle escape when  $R_{\text{cor}}/\ell_c \sim O(1)$ . Pair loading tends to increase the Alfvénic velocity and the proton temperature (assuming  $\beta_p \sim 1$ ), yet it exerts a small influence on the overall turbulent magnetic energy density.

In the present paper, we do not model the physics of electron energization, which is governed by fast processes acting on timescales well below those controlling proton acceleration, e.g. reconnection in microscopic current sheets (e.g., Beloborodov 2017). Furthermore, a detailed modelling of the electron energy distribution requires a detailed treatment of radiative interactions for mildly relativistic electrons (e.g., Coppi 1992; Belmont et al. 2008; Veledina et al. 2011), which we postpone to a further study, as this does not otherwise impact the proton spectra that we seek to determine. We rather assume that this distribution is characterized at all times by a Maxwellian with dimensionless temperature  $\Theta_e \equiv k_B T_e / (m_e c^2) \sim 0.2$ . Such a distribution, in the rest frame of the central black hole, could also arise from Doppler broadening by strong turbulent motions, even if the electrons remain cool in the local comoving frame of the turbulent plasma (Beloborodov 2017; Sironi & Beloborodov 2020; Groselj et al. 2024).

Our framework accounts for inverse Compton energization of soft disk photons, that shapes the X-ray spectrum responsible for  $p\gamma$  interactions at the origin of the high-energy neutrinos. To model the injection spectrum of soft photons in the corona, we approximate the accretion-disk emission with a multicolour blackbody spectrum, taking the spectral luminosity per unit energy as  $L_\epsilon^{\text{disk}} \propto \epsilon^3$  for  $\epsilon < 0.1 \epsilon_d$  and  $L_\epsilon^{\text{disk}} \propto \epsilon^{4/3} \exp(-\epsilon/\epsilon_d)$  for  $\epsilon \geq 0.1 \epsilon_d$ , with a characteristic cutoff  $\epsilon_d = 31.5 \text{ eV}$ . Due to geometrical and opacity effects, the corona intercepts only a fraction  $f_{\text{cor}} \sim 0.2$  of the disk luminosity  $L_d$  (e.g., Ghisellini & Tavecchio 2009; Dovčiak et al. 2022).

This physical environment, combining hot ions, sub-relativistic electrons, strong magnetic fields, dynamic turbulence and a strong radiation field provides favorable conditions for the stochastic acceleration of charged particles and for the production of multi-wavelength and multi-messenger emission.

### 2.2. Stochastic acceleration of protons

In magnetized turbulent coronae, stochastic proton acceleration mediated by repeated interactions between charged particles and the turbulent electric fields provides a natural pathway to acceleration. The efficiency of subsequent turbulent acceleration is governed by two factors, which remain insufficiently constrained today: the fraction of protons extracted from the thermal population and injected into the non-thermal component, and the properties of the turbulent energization mechanism

itself. Regarding the latter, stochastic particle acceleration is commonly described in the framework of a quasi-linear theory of resonant wave-particle interactions (e.g., [Schlickeiser 2002](#), and references therein) and numerically modelled using a purely diffusive Fokker-Planck scheme. However, this scheme appears to disagree with recent magnetohydrodynamic (MHD) and PIC simulations, see e.g. [Zhdankin et al. \(2017\)](#); [Comisso & Sironi \(2019\)](#); [Kimura et al. \(2019\)](#); [Wong et al. \(2020\)](#); [Trotta et al. \(2020\)](#); [Bresci et al. \(2022\)](#); [Pezzi et al. \(2022\)](#); [Meringolo et al. \(2023\)](#); [Pugliese et al. \(2023\)](#); [Wong et al. \(2025\)](#), and [Lemoine & Malkov \(2020\)](#) for a discussion of these issues. This has spurred new theoretical ideas on modelling stochastic acceleration in strongly turbulent plasmas (e.g., [Lynn et al. 2014](#); [Lemoine 2019](#); [Lemoine & Malkov 2020](#); [Demidem et al. 2020](#); [Sioulas et al. 2020a,b](#); [Lemoine 2021, 2022](#); [Xu & Lazarian 2022](#); [Das et al. 2025](#); [Lemoine 2025](#)). Here we remain agnostic and envisage several prescriptions for modelling transport in momentum space, including the standard Fokker-Planck approach employing a diffusion coefficient extracted from PIC simulations and a generalized description of Fermi acceleration ([Lemoine 2022](#)).

In relativistic turbulence, magnetic reconnection in microscopic current sheets acts as the injection mechanism ([Comisso & Sironi 2019](#)). It extracts a significant fraction of protons from the thermal pool and pre-accelerates them before they undergo stochastic energization by turbulent magnetic fields. The turbulent magnetization parameter is defined as  $\sigma_{\delta B} = \delta B^2 / (4\pi n_p m_p c^2)$ , also written as the Alfvén 4-velocity squared  $\sigma_{\delta B} = (v_A/c)^2 / [1 - (v_A/c)^2]$ . For reference, [Comisso & Sironi \(2019\)](#) report an injected particle fraction of  $\xi_{n_p} \sim 0.2 - 0.3$  at  $\sigma_{\delta B} \sim 10$ , where  $\xi_{n_p} \equiv n_{p,\text{nth}}/n_{p,\text{tot}}$  denotes the number fraction of particles injected into the non-thermal population. In terms of pressure ratio between non-thermal and thermal particles, hereafter  $\xi_p \equiv (P_{p,\text{nth}}/P_{p,\text{tot}})$ , this implies  $\xi_p$  close to unity. However, these fractions, and possibly the injection mechanism itself, may vary in mildly or sub-relativistic regimes ([Comisso & Sironi 2022](#); [Wong et al. 2025](#)). Consequently, within our mildly relativistic framework ( $\sigma_{\delta B} \sim 0.1$ ), we treat the injection fraction  $\xi_p$  as a free parameter. We adopt a fiducial value of  $\xi_p = 0.1$  and assume that particles are injected at  $\epsilon_{p,\text{inj}} = \mathcal{O}(m_p c^2)$ . The key parameter is here  $\xi_p$ , not  $\epsilon_{p,\text{inj}}$ , whose exact value does not exert a strong influence on the final spectra. Since  $\xi_p/\xi_{n_p} \simeq \epsilon_{p,\text{inj}}/k_B T_p$ , this choice of  $\xi_p$  corresponds to  $\xi_{n_p} \sim 10^{-2}$ . We discuss the influence of  $\xi_p$  on our results in [Sec. 3.2](#).

The acceleration of the non-thermal proton spectral density  $\mathcal{N}_p \equiv dN_p/dp = 4\pi p^2 f(p, t)$  (with  $f$  the distribution function and  $N_p$  the number density of protons) is modelled with a transport equation including an operator describing the stochastic acceleration, whose form depends on the physical regime considered. Here, we focus on the differential operator modelling this evolution in momentum space, and discuss in [Sec. 2.3](#) the full transport equation for protons (and other species).

For small-amplitude, quasi-linear type interactions, we follow standard treatments and describe the diffusion process using a purely diffusive Fokker-Planck equation for momentum  $p$ ,

$$\mathcal{L}_{\text{FP}} \mathcal{N}_p \equiv \partial_p (D_{pp} \partial_p \mathcal{N}_p) - 2 \partial_p \left( \frac{D_{pp}}{p} \mathcal{N}_p \right), \quad (4)$$

characterized by the diffusion coefficient  $D_{pp}$ . We also use  $D_{pp} = 0.3 \sigma_{\delta B} p^2 c / \ell_c$  as obtained from numerical PIC simulations in the relativistic regime  $\sigma_{\delta B} \gtrsim 1$ . Recently, [Wong et al. \(2025\)](#) has reported a different scaling in the sub-relativistic regime  $\sigma_{\delta B} <$

1,  $D_{pp} \propto \sigma_{\delta B}^{3/2}$  and confirmed that, in order to reproduce the observed energy distributions, one needs to introduce a net advection coefficient with a non-trivial energy dependence. In light of this discrepancy, and noting that an order of unity modification in the diffusion coefficient translates in a similar renormalization of the magnetization, we retain the above value of  $D_{pp}$  and compare in [Appendix A](#) our different schemes of stochastic acceleration to evaluate the impact on the neutrino spectra. In this regime, the acceleration rate is given by  $v_{\text{acc}}(p) = t_{\text{acc}}(p)^{-1} = 4D_{pp}/p^2$ .

In strongly turbulent coronae, where  $\delta B/B_0 \gtrsim 1$  ( $B_0$  background field,  $\delta B$  characteristic turbulent amplitude), the acceleration process is influenced by the intermittency of the turbulent fluctuations. To describe this regime, we rely on the transport equation introduced in [Lemoine \(2022\)](#), which was successfully benchmarked on the results of MHD simulations at  $v_A/c \simeq 0.4$ , close to the range that we investigate. The corresponding differential operator reads

$$\mathcal{L}_{\text{GF}} \mathcal{N}_p \equiv \int_0^\infty 2\pi c \left[ \mathcal{N}_{p'} \frac{\varphi(p|p')}{l_g(p')} - \mathcal{N}_p \frac{\varphi(p'|p)}{l_g(p)} \right] dp', \quad (5)$$

where  $\varphi(p|p')$  is the transition probability of momentum  $p'$  to jump to momentum  $p$ , and  $l_g(p) \equiv 2\pi pc/eB$  is the gyroradius scale of the particle. This master-type operator allows for non-local transfers in momentum space and captures regimes where interactions induce finite or large momentum jumps. It describes a ‘‘generalized Fermi’’ process, in which protons can gain or lose energy as they cross intermittent regions of dynamic, curved and/or compressed magnetic field lines. In this formalism, energization results from the crossing of velocity gradients  $\Gamma_{l_g}$ , proceeding according to  $\dot{p} = \Gamma_{l_g} p$ , implying an acceleration rate  $v_{\text{acc}}(p) = t_{\text{acc}}(p)^{-1} = \langle \Gamma_{l_g}(p) \rangle$ . For a recent application to the modelling of the spectral energy distribution of microquasars, see [Dmytriiev et al. \(2026\)](#).

If a substantial fraction of the turbulent energy is dissipated into the proton non-thermal component, as is suggested by the high neutrino luminosity inferred from IceCube observations of Seyfert galaxies, the energy lost by the cascade must be accounted for. This backreaction process alters the cascade, therefore the acceleration process, and thus eventually the proton spectra. This implementation is discussed in [Sec. 2.6](#).

### 2.3. Transport equation for various species

For each particle species  $s$  considered here (mainly protons, leptons, photons and neutrinos, but also pions and muons), the evolution of the particle density spectrum  $\mathcal{N}_s \equiv dN_s/dp$  is described by a transport equation of the form

$$\partial_t \mathcal{N}_s = [\mathcal{L}_{\text{stoch}} \mathcal{N}_s]_{s=p} - \partial_p (p v_{\text{loss}} \mathcal{N}_s) - \frac{\mathcal{N}_s}{t_{\text{esc},s}} + Q_s, \quad (6)$$

with the following definitions. First, the terms in brackets only applies for protons, as it represents stochastic acceleration; as explained in [Sec. 2.4](#), we do not treat here the dynamical evolution of the electron/positron population, which evolves on short timescales. The operator  $\mathcal{L}_{\text{stoch}}$  corresponds to the differential operator  $\mathcal{L}_{\text{FP}}$  or  $\mathcal{L}_{\text{GF}}$  described earlier. The second term on the right hand side describes systematic momentum losses due to interactions through the rate  $v_{\text{loss}}$ , further discussed in [Sec. 2.4](#). The third term parametrizes particle removal, either through diffusive escape from the corona ([Sec. 2.5](#)), annihilation (for pairs and photons), hadronic interactions (for protons) and decay (pions and muons). The source term  $Q_s$  accounts for particle in-

Table 1: Physical processes included in the transport equation for each particle species for our framework.

Particle	Stochastic acceleration $\mathcal{L}_{\text{stoch}}$	Energy losses $\partial_p(p\nu_{\text{loss}}N)$	Escape $N/t_{\text{esc}}$	Source term $\mathcal{Q}$
Protons	Yes ( $\mathcal{L}_{\text{FP,GF}}$ )	$pp$ , $p\gamma$ , Bethe Heitler	Diffusion	Injection
Leptons ( $e^-, e^+$ )	Neglected	Synch., IC	Diffusion	$e^-$ : Injection, $e^\pm$ : $\gamma\gamma/\text{BH}$ pair creation
Photons	-	-	Eff. light crossing, $\gamma\gamma$ absorption	Disk radiation, radiative emission
Neutrinos	-	-	Light crossing	$\pi^\pm, \mu^\pm$ decays
Pions / Muons	Neglected	Neglected	Disintegration	Hadronic interactions

jection (for protons and electrons), or production through interactions, e.g. annihilation (pairs and photons) and radiative processes (pions, muons and neutrinos). These various processes and their corresponding implementation are described in detail in [Klinger et al. \(2024\)](#). Depending on the particle species and the physical processes involved, some of these terms may be absent or take different explicit forms. A summary of the transport terms retained for each species in our model is given in Table 1.

As in [Lemoine & Rieger \(2025\)](#), we integrate the above transport equations up to time  $t_{\text{adv}}$ , which characterizes the crossing time of the corona by advection with the background plasma at velocity  $v_{\text{adv}}$ , as described in Sec. 2.5. This describe an inflow of the corona plasma but it could also describe an outflow, for example in a jetted corona. The overall proton spectral shape is governed by the influence of radiative losses (mostly at the highest energies), the consequence of turbulent damping, and the relative importance of acceleration, escape, and advection processes. This interplay can be conveniently characterized by the ratios of timescales

$$\frac{t_{\text{esc}}}{t_{\text{acc}}} \approx \left(\frac{R_{\text{cor}}}{\ell_c}\right)^2 \frac{v_A}{c}, \quad \frac{t_{\text{adv}}}{t_{\text{acc}}} \approx \frac{R_{\text{cor}}}{\ell_c} \frac{v_A^2}{v_{\text{adv}}c}. \quad (7)$$

Large values of  $t_{\text{esc}}/t_{\text{acc}}$  imply efficient confinement, allowing protons to undergo multiple acceleration cycles and build up a hard, extended non-thermal spectrum. Conversely, when  $t_{\text{esc}}/t_{\text{acc}} \ll 1$ , escape dominates over acceleration, leading to a suppressed high-energy proton population and neutrino production. The second ratio,  $t_{\text{adv}}/t_{\text{acc}}$ , controls the maximum energy that protons can achieve before being advected out of the corona, into the black hole or in the jet. For  $t_{\text{adv}}/t_{\text{acc}} \ll 1$ , advection removes particles faster than they can be accelerated, and the proton spectrum exhibits a high-energy cutoff controlled by advection, i.e. by the maximum time over which acceleration can take place. In contrast, when  $t_{\text{adv}}/t_{\text{acc}} \gtrsim 1$ , protons have sufficient time to reach energies at which radiative and photohadronic losses become dominant.

#### 2.4. Radiative and hadronic losses and timescales

Particles experience systematic energy losses through radiative and hadronic processes. The relevant timescales are shown in Fig. 1 for protons, electrons, and photons, as computed with AM3 for a fiducial configuration in which the disk luminosity is  $L_d = 5.0 \times 10^{44} \text{ erg s}^{-1}$ , the corona has a characteristic size  $R_{\text{cor}} = 15 r_g$ ,  $\tau_T = 0.5$ ,  $n_p/n_e = 1$ ,  $\xi_p = 0.1$ ,  $\ell_c = 4.0 r_g$ , and  $v_A = 0.25 c$ . For comparison, the escape and acceleration timescales are also displayed.

Protons and electron-positron pairs in the corona lose energy through interactions with the ambient magnetic and radiation fields, as well as through hadronic and other plasma processes. Given the compactness  $\ell_{\text{comp}} \equiv 4\pi(m_p/m_e)(L_d/L_{\text{edd}})(r_g/R_{\text{cor}}) \approx$

$50 L_{\text{d},44} (R_{\text{cor}}/15 r_g)^{-1} M_{7,2}^{-1}$ , with  $L_{\text{edd}}$  the Eddington luminosity, and given the plasma magnetization  $\sigma_B \approx 0.1(B/5 \times 10^3 \text{ G})^2 (R_{\text{cor}}/15 r_g) x_p^{-1} (\tau_T/0.5)^{-1}$ , we see that the pairs cool efficiently through synchrotron and inverse Compton losses. In detail, inverse Compton losses of electrons with Lorentz factor  $\gamma_e = \varepsilon_e/m_e c^2$  occur on  $t_{\text{IC,e}} = 3R_{\text{cor}}/(4\gamma_e \ell_{\text{comp}} c) \approx 0.02(R_{\text{cor}}/c) (\ell_{\text{comp}}/50)^{-1} (\varepsilon_e/600 \text{ keV})^{-1} \ll R_{\text{cor}}/c$ , and similarly for synchrotron losses,  $t_{\text{syn,e}} = (3m_e/2m_p) R_{\text{cor}}/(\gamma_e \sigma_B c) \approx 0.02(R_{\text{cor}}/c) (\sigma_B/0.1)^{-1} (\varepsilon_e/600 \text{ keV})^{-1} \ll R_{\text{cor}}/c$ . This justifies our approximation of fixing the electron distribution function to its steady state Maxwellian shape on the timescales of proton evolution, that are larger than  $R_{\text{cor}}/c$ . For comparison, the typical acceleration timescale for stochastic acceleration reads

$$t_{\text{acc}} \approx 4 \frac{R_{\text{cor}}}{c} \left(\frac{v_A}{0.25c}\right)^{-2} \left(\frac{\ell_c}{5r_g}\right). \quad (8)$$

Protons within the corona lose momentum through the following radiative and hadronic processes: synchrotron radiation, inverse Compton scattering, inelastic proton-proton ( $pp$ ) collisions, photohadronic ( $p\gamma$ ) interactions, and Bethe-Heitler (BH) pair production. However, proton synchrotron and inverse Compton losses can be neglected in the conditions of AGN coronae, as their timescales are  $(m_p/m_e)^4$  larger than the corresponding electron loss timescales. Proton losses are dominated by the hadronic ( $pp$ ,  $p\gamma$ ) and Bethe-Heitler channels ([Murase et al. 2020](#); [Eichmann et al. 2022](#); [Das et al. 2024](#)). More specifically, our detailed numerical computations using AM3 indicate that  $pp$  interactions dominate for protons below 1 TeV, that BH pair production,  $pp$  and  $p\gamma$  interactions are all relevant in the range between 1 and 10 TeV, while  $p\gamma$  eventually dominates above 10 TeV, see Fig. 1. For our fiducial parameters, the proton cooling timescale falls below the acceleration timescale at energies  $\gtrsim 10 \text{ TeV}$ , as required to produce the 1–10 TeV neutrinos observed by IceCube. For photons, the  $\gamma\gamma$ -annihilation timescale computed with AM3, shown in Fig. 1, becomes shorter than the photon escape timescale for energies above  $\sim 100 \text{ keV}$ . High-energy gamma-ray photons are thus efficiently absorbed and reprocessed within the corona. In contrast, neutrinos escape freely, so their flux remains unaffected and can exceed the observed photon flux at TeV energies. Finally, pion and muon energy losses and acceleration can be safely neglected, as their typical decay timescales are much shorter than any radiative or hadronic cooling timescale.

#### 2.5. Spatial transport in the corona

Protons, electrons, positrons, and other charged particles can escape from the corona on a characteristic diffusive timescale  $t_{\pm, \text{esc}} = R_{\text{cor}}^2/(2\kappa)$ , with spatial diffusion coefficient  $\kappa$ . This coefficient includes both turbulent diffusion by advection with the large-scale eddies and pitch-angle scattering on magnetic inhomogeneities in the comoving frame. The turbulent contribution

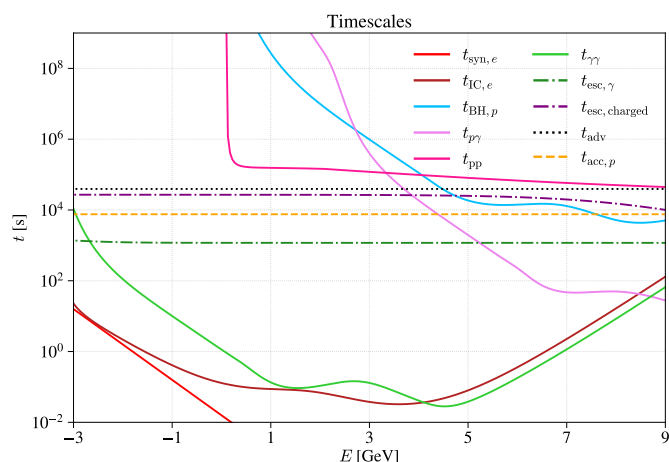


Fig. 1: Timescales of the different processes occurring in the AGN corona, including the escape of charged and neutral particles, the acceleration of protons, radiative and hadronic losses of protons and electrons/positrons,  $\gamma\gamma$  annihilation of photons and the advection timescale of the coronal plasma.

is approximated as  $\kappa_{\text{turb}} \simeq \ell_c v_A/3$ , in agreement with recent PIC simulation results (Groselj et al. 2026), while the scattering contribution is taken as  $\kappa_{\text{scatt}} \simeq r_L^{1/3} \ell_c^{2/3} c/3$ , see e.g. Berezhinskii et al. (1990); Schlickeiser (2002) or for recent studies in large amplitude turbulence Kempfski et al. (2023); Lemoine (2023). The total diffusion coefficient,  $\kappa = \kappa_{\text{turb}} + \kappa_{\text{scatt}}$ , therefore leads to a momentum-dependent escape timescale for charged particles.

We also assume that the plasma is advected through the corona with characteristic velocity  $v_{\text{adv}}$ . This transport characterizes advection into the central black hole, but it can also model advection along an outflow in models where the corona lies on a jet boundary (Sridhar et al. 2025). We assume here a velocity describing radial advection (see Shakura & Sunyaev 1973; Frank et al. 2002)

$$v_{\text{adv}}(r) \simeq \alpha v_K(r) = \alpha c \hat{r}^{-1/2}, \quad (9)$$

where  $\alpha \simeq 0.1$  is the accretion viscosity parameter,  $v_K(r)$  is the Keplerian velocity, and  $\hat{r} \equiv r/r_g$ . For a corona of size  $R_{\text{cor}} = 15 r_g$ , the advection speed at the outer boundary typically reaches  $v_{\text{adv}}(R_{\text{cor}}) \simeq 0.03 c$ .

Protons are assumed to be continuously injected at the outer edge of the corona and are subsequently transported by advection, until they are advected out of the corona. In this configuration, the temporal evolution of a particle population is directly mapped onto its radial evolution through  $dt = dr/v_{\text{adv}}(r)$  so that the time-dependent spectrum of a particle can equivalently be described as a function of its radial position in the corona. As discussed in Lemoine & Rieger (2025), this method also provides a satisfactory model of the case in which protons are continuously injected at all points in the corona, at least as long as the corona is treated as one-zone.

In this work, we adopt the simplifying approximation of a constant advection velocity throughout the corona,  $v_{\text{adv}}(r) \simeq v_{\text{adv}}(R_{\text{cor}})$ . Under this assumption, the advection timescale reduces to  $t_{\text{adv}} \equiv R_{\text{cor}}/v_{\text{adv}}$ , so that the spatially averaged proton spectrum can be expressed as a simple time average,

$$\mathcal{N}_{p,\text{cor}} = \frac{1}{t_{\text{adv}}} \int_0^{t_{\text{adv}}} \mathcal{N}_p(t) dt. \quad (10)$$

The distributions  $\mathcal{N}_p(t)$  are obtained as the time-dependent solutions of the transport equation Eq. (6).<sup>1</sup>

Although the assumption of a constant advection velocity is clearly idealized, its impact on the results is partially mitigated by the fact that a stronger turbulence and magnetic amplification closer to the black hole are expected to increase the Alfvén speed  $v_A$ , which would in turn boost the acceleration rate. This effect act in opposite direction of the increase of  $v_{\text{adv}}$  close to the black hole and they tend to partially compensate each other. Detailed information from radiative GRMHD simulations of accreting BH would be highly valuable in that respect, and could be incorporated into the present framework. The advection timescale (Fig. 1) sets an upper limit on the available time for acceleration, unlike  $t_{\text{esc}}$ , which characterizes a stochastic process of escape.

## 2.6. Turbulent cascade and damping by energetic particles

Matching the neutrino flux observed by IceCube requires a non-thermal proton energy density comparable to the magnetic energy density in the corona (Das et al. 2024). Furthermore, the energy fraction of the non-thermal population  $\xi_p$  inferred in relativistic (Comisso & Sironi 2019) and mildly relativistic (Comisso & Sironi 2022) PIC simulations indicate that the energy density in non-thermal protons can become comparable to the magnetic pressure. Under these conditions, the dissipation of turbulent energy into particle acceleration becomes potentially significant with regards to the flow of turbulent energy through the cascade, implying substantial damping of turbulent power. A self-consistent description of the dissipation of turbulent energy and its impact on particle acceleration is therefore an important and well-motivated ingredient of our model.

The co-evolution of stochastic acceleration and turbulence dissipation has been addressed in various astrophysical contexts in recent years (e.g., Kakuwa 2016; Sciacaluga & Tavecchio 2022; Gong et al. 2025). To describe this non-linear interplay, we follow the general treatment of Lemoine et al. (2024) and Lemoine & Rieger (2025). We assume that the turbulent fluctuations are characterized by a power spectrum  $S_k \propto k^{-5/3}$  in terms of wavenumber  $k$ , with  $\mathcal{E}_{B_k} \propto k S_k \propto k^{-2/3}$ , and overall normalisation  $\int d \ln k \mathcal{E}_{B_k} = \delta B^2/8\pi$ . Energy is injected at the correlation scale  $\ell_c \sim k_{\text{inj}}^{-1}$  and cascades through the inertial range ( $k_{\text{inj}} \ll k \ll k_{\text{diss}}$ ) with a constant flux  $\gamma_k \mathcal{E}_{B_k}$ , where  $\gamma_k \propto k^{2/3}$ . To model the dissipation of turbulent power – strictly speaking, of the turbulent electric fields – by particle acceleration, we introduce a kernel  $\phi(k, p)$  that specifies how turbulence at wavenumber  $k$  feeds particles of momentum  $p$ . The cascade equation is therefore

$$\partial_t \mathcal{E}_{B_k} = -k \partial_k (\gamma_k \mathcal{E}_{B_k}) - \int \phi(k, p) \varepsilon_p p \partial_t \mathcal{N}_p(p, t) d \ln p, \quad (11)$$

guaranteeing overall energy conservation between the proton non-thermal energy distribution and the turbulence spectrum at a given point, thanks to the normalization property  $\int d \ln k \phi(k, p) = 1$ . For simplicity, we assume that  $\phi(k, p)$  describes interactions at  $k \sim (eB/pc)$ , as characterized by a Gaus-

<sup>1</sup> Equation (10) implicitly assumes that particles are confined in, and advected with the plasma in ballistic motion, i.e.,  $t_{\text{esc}} \gg t_{\text{adv}}$ . It remains valid in the opposite limit  $t_{\text{adv}} \gg t_{\text{esc}}$ , when advection does not play any significant role. In such a case, the limit  $t_{\text{adv}} \rightarrow +\infty$  can be taken, and Eq. (10) then provides the steady-state solution to the transport equation. In the intermediate limit  $t_{\text{adv}} \sim t_{\text{esc}}$ , it remains a satisfactory approximation, as we have checked using a simple Monte-Carlo model describing spatial transport, neglecting particle energization.

sian centered at  $(\ln k + \ln(pc/eB))$  and normalized to unity. This choice does not affect our conclusions, as discussed in the above references. Conversely, the damping of the cascade reduces the efficiency of stochastic acceleration, as modelled through the time-dependent acceleration rate

$$v_{\text{acc}}(p, t) = v_{\text{acc}}(p, t = 0) a \int \phi(k, p) \mathcal{E}_{B_k}(t) d \ln k, \quad (12)$$

with  $a = \left( \int \phi(k, p) \mathcal{E}_{B_k}(t = 0) d \ln k \right)^{-1}$  a normalization coefficient. The time-dependent acceleration rate enters Eq. (6) through the diffusion coefficient or the velocity gradients, as discussed in Sec. 2.2.

In practice, damping becomes significant when the power injected into particles competes with the turbulent energy flux. Utilizing the acceleration frequency  $v_{\text{acc}} \approx v_A^2/(c\ell_c)$  and the cascade rate  $\gamma_{\text{kinj}} \approx f_{\text{diss}} v_A/\ell_c$ , and substituting  $\mathcal{E}_{B_{\text{kinj}}} \approx \delta B^2/(8\pi) = P_{\text{th}}/\beta_p$ , the condition for the onset of damping reads:

$$u_{p, \text{non-th}}(t) \sim \frac{f_{\text{diss}} P_{\text{th}}}{v_A/c \beta_p}. \quad (13)$$

Once damping sets in, proton acceleration slows down. In practice, if the cascade is quenched at wavenumber  $k_{\text{damp}}$ , only particles with gyroradius  $r_L = pc/eB > k_{\text{damp}}^{-1}$  continue to be accelerated, and their energy gain is limited by the turbulent energy available at  $k_{\text{damp}}$ . Beyond that point, the proton energy spectrum flattens out to equal energy per decade, meaning approximately  $dN_p/d\varepsilon_p \propto \varepsilon_p^{-2}$ . As a result, the maximum non-thermal energy density is here limited to a characteristic value close to the turbulent and plasma pressure.

## 2.7. Numerical set-up

The numerical strategy implemented in Turb-AM3 aims at solving self-consistently the momentum-space transport equation for protons [Eq. (6)] together with the turbulent cascade equation [Eq. (11)], while all other particle species (electrons, positrons, photons, neutrinos, muons, and pions) are evolved with the standard AM3 solver, Eq. (6) without the acceleration term.

The physical state of the corona is specified by a set of characteristic parameters: the mass of the central supermassive black hole  $M_{\text{BH}}$ , the coronal radius  $R_{\text{cor}}$ , the bolometric luminosity of the accretion disk  $L_d$ , the magnetic-field strength  $\delta B \sim B$ , the turbulence coherence length  $\ell_c$ , and the advection velocity  $v_{\text{adv}}$ . The electron density  $n_e$  is chosen such that the optical depth is of order unity, then the proton density is determined via the proton-to-lepton density ratio  $n_p/n_e$ . We also specify the proton and electron temperatures,  $T_p$  and  $T_e$ , and the initial energy fraction between non-thermal and total protons,  $\xi_p$ . The stochastic acceleration mechanism implemented in the simulation is determined by selecting the appropriate transport operator from among  $\mathcal{L}_{\text{FP}}$  and  $\mathcal{L}_{\text{GF}}$ ; the distribution function can also be evolved by a pure advection process characterizing Fermi-I acceleration, but we do not consider it here. Finally, we define numerical quantities including the grid in momentum space and the timestep, the latter of which is taken as a fraction of the characteristic light-crossing time  $\ell_c/c$ .

The initial particle populations are then constructed as follows. Electrons are injected following a thermal Maxwell-Jüttner distribution at a temperature  $T_e$ , normalized to the electron density  $n_e$ . Non-thermal protons are initialized with a power-law shape  $dN_p/dp \propto p^{-4}$  as observed for stochastic acceleration in the sub-relativistic regime (Comisso & Sironi 2022; Lemoine

2022), with  $p_{\text{min}} = m_p c$  and  $p_{\text{max}} = 5 \times 10^8$  GeV, but the precise parametrization does not have an impact on the final proton spectrum. Their initial total pressure is normalized to  $\xi_p P_{\text{th}}$ . The photon field is initialized as a multi-temperature blackbody spectrum representing the disk radiation field. While the injection remains constant in time, the photon population evolves dynamically through all included radiative, hadronic, and pair-production processes.

At each timestep, the non-thermal proton distribution is advanced by computing a full step of stochastic acceleration (Eq. (6) without escape, injection and losses), and turbulent damping [Eq. (11)]. This requires solving the modified turbulent cascade equation, including backreaction from the energetic particles through the kernel  $\phi(k, p)$ , and computing the associated effective acceleration rate defined by Eq. (12). The resulting proton spectral energy density is interpolated from momentum space onto the AM3 energy grid. The AM3 radiative solver then advances all species, using the updated proton spectrum as input, and taking into account losses and escape, Eq. (6) without the acceleration term. The updated spectra of all species are stored, and the proton spectrum is passed to the next acceleration step.

The electron population is taken to be constant in time, as it evolves on short timescales such that steady-state is a satisfactory approximation. For photons, we emphasize that initially only the disk photon distribution is an input. The X-ray component is a consequence of the inverse Compton scattering of the soft photons of the disk by the sub-relativistic thermal electrons, and is computed with the AM3 code.

The duration of one simulation is  $t_{\text{adv}}$ . The average particle populations of all species over the corona volume are computed as in Eq. (10). This average represents the stationary spectrum of the corona, and must be distinguished from the time-dependent spectra of each particle species at different points in the corona.

## 3. Multi-messenger emission from NGC1068

### 3.1. Fiducial parameter set

We now apply Turb-AM3 to compute the photon and neutrino spectra from NGC 1068 for our fiducial set of parameters:  $L_d = 5.0 \times 10^{44}$  erg s<sup>-1</sup>,  $R_{\text{cor}} = 15 r_g$ ,  $\tau_T = 0.5$ ,  $\xi_p = 0.1$ ,  $\ell_c = 4.0 r_g$ ,  $v_{\text{adv}} = 0.03 c$ , and  $v_A = 0.25 c$ . These parameters are consistent with previous studies (Das et al. 2024; Lemoine & Rieger 2025; Yuan et al. 2026). Stochastic acceleration of protons is here modelled using the diffusive acceleration scheme (Eq. 4). Alternative acceleration prescriptions are discussed in Appendix A.

The resulting multi-messenger spectra are plotted in Fig. 2, which shows that the observed IceCube neutrino flux is satisfactorily reproduced by this standard set of parameters, and that it remains consistent with the  $\gamma$ -ray constraints. This is a notable result that supports previous semi-analytical estimates. Note that Fig. 2 includes two different IceCube reconstructions of the neutrino signal (see Abbasi et al. 2025b, 2026). The first (pink) corresponds to a phenomenological fit assuming a simple power-law spectrum, while the second (purple) is obtained under the assumption of a disk-corona emission model presented by Murase et al. (2020); Kheirandish et al. (2021). Since the disk-corona model spectrum provides a more physically motivated comparison with our model than a generic power-law, we focus on the latter (purple) dataset.

The stationary proton spectrum (inset of Fig. 2) is relatively flat and the integrated energy density lies close to the background plasma pressure. Both features arise from the self-regulation in-

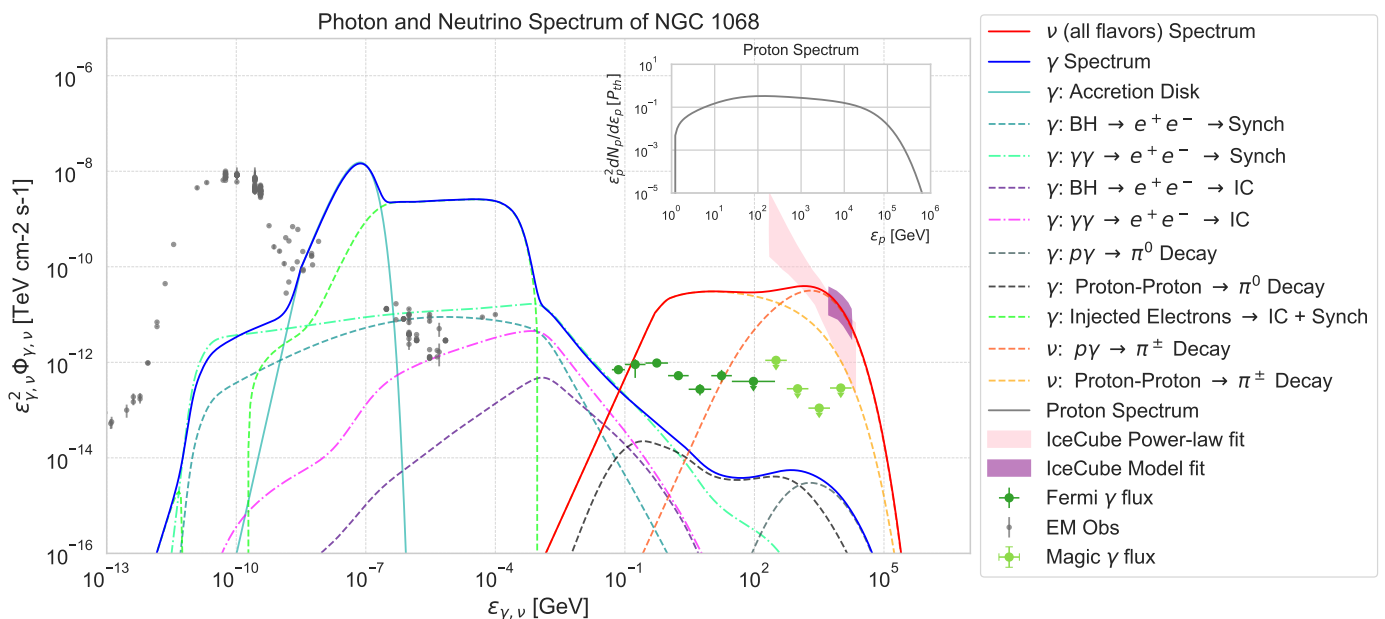


Fig. 2: Photon (blue) and neutrino (red) spectra from NGC 1068 computed with Turb-AM3 for a fiducial set of parameters:  $L_d = 5.0 \times 10^{44} \text{ erg s}^{-1}$ ,  $R_{\text{cor}} = 15 r_g$ ,  $\xi_p = 0.1$ ,  $\ell_c = 4.0 r_g$ ,  $v_{\text{adv}} = 0.03 c$ , and  $v_A = 0.25 c$ . The contributions from the different radiative and interaction processes are shown separately. BH denotes Bethe–Heitler pair production,  $\gamma\gamma$  indicates photon–photon self-absorption, and IC refers to inverse Compton scattering. All spectra are shown as fluxes observed at Earth, assuming a luminosity distance of 10 Mpc. Neutrino data from IceCube (Abbasi et al. 2026) and electromagnetic observations (Chang et al. 2020; The Fermi Collaboration 2020; MAGIC Collaboration et al. 2019) are included for comparison. The stationary proton spectrum obtained with Turb-AM3 is displayed in grey in the inset, where the energy distribution is normalized to the background plasma pressure  $P_{\text{th}}$ .

duced by the back-reaction of accelerated protons on the turbulent cascade. A cutoff appears at a few tens of TeV, corresponding to the energy at which photohadronic losses become dominant over acceleration (see Fig. 1). The associated neutrino spectrum (red curve in Fig. 2) reflects the underlying proton distribution. The  $pp$  component is approximately flat and dominates at low energies ( $\sim 1\text{--}100 \text{ GeV}$ ). At higher energies ( $\sim 1\text{--}30 \text{ TeV}$ ), neutrino production is dominated by photohadronic ( $p\gamma$ ) interactions, highlighting the crucial role of the coronal X-ray photon field, as noted in earlier studies. Protons at tens of TeV efficiently produce neutrinos in the 3–30 TeV range observed by IceCube, making the  $p\gamma$  threshold a natural explanation for the characteristic neutrino energies.

Figure 2 also shows that Turb-AM3 reproduces the main features of the coronal X-ray spectrum, arising from inverse Compton scattering of disk photons by thermal electrons. For typical coronal conditions (Rybicki & Lightman 1979), the X-ray luminosity spectrum expected from thermal Comptonization can be approximated as

$$L_{X,\varepsilon} \propto \varepsilon^2 \frac{dN_\gamma}{d\varepsilon} \propto \varepsilon^{(\ln \tau_T / \ln A) + 1} \exp\left(-\frac{\varepsilon}{k_B T_e}\right), \quad (14)$$

where  $\tau_T$  is the Thomson optical depth and  $A = 1 + 4k_B T_e / (m_e c^2)$  is the average energy amplification factor per scattering. For  $\tau_T \lesssim 1$  and  $A \gtrsim 1$ , this expression yields an approximately flat spectrum extending up to an exponential cutoff at  $\varepsilon \sim k_B T_e \sim 100 \text{ keV}$ . Our results are consistent with this expectation: disk photons are efficiently up-scattered, producing a hard power-law X-ray spectrum with a high-energy cutoff at a few hundred keV. We note that AM3 calculates a time-dependent photon distribution through repeated inverse Compton calculations, and that this distribution rapidly reaches the above equilibrium spectrum. In the

current version, the electron distribution around the thermal peak is not finely resolved by the numerical grid. While the current implementation provides a satisfactory description of the X-ray emission, a more accurate treatment of thermal Comptonization will be addressed in future work.

High-energy  $\gamma$  rays produced in hadronic interactions initiate an electromagnetic cascade in the dense photon field of the corona. Absorption through  $\gamma\gamma \rightarrow e^+e^-$  pair production generates secondary pairs that cool via synchrotron and inverse Compton emission, producing additional photons and sustaining the cascade. As a result, the initial TeV  $\gamma$ -ray power is redistributed to lower energies, suppressing the direct escape of TeV photons. This reprocessing is visible in Fig. 2, where a broad cascade extends from  $\sim 1 \text{ MeV}$  to  $\sim 1 \text{ GeV}$ . The pair density produced by the cascade is  $n_{\text{pairs}} \simeq 5.0 \times 10^6 \text{ cm}^{-3}$ , much smaller than the primary electron density  $n_{e^-} \simeq 2.2 \times 10^{10} \text{ cm}^{-3}$ . Pair production therefore remains dynamically negligible and does not significantly modify the electron distribution, validating the assumption  $n_{e^\pm} \approx n_{e^-}$  throughout the evolution.

Accordingly, the predicted high-energy gamma-ray spectrum lies below the observed level of emission, whose origin is rather attributed to the extended starburst region (e.g., Ajello et al. 2023). At lower energies ( $\lesssim 1 \text{ MeV}$ ), disk and coronal photons are absorbed and reprocessed by the dusty torus. Within these constraints, our model reproduces the IceCube neutrino flux without violating  $\gamma$ -ray limits, consistent with Das et al. (2024).

To ensure the physical viability of the model, we performed a comprehensive consistency check of the energy budget. The total coronal + disk photon luminosity is  $L_{\gamma,\text{tot}} = 7.6 \times 10^{44} \text{ erg s}^{-1}$ , which remains below the Eddington limit ( $L_{\text{edd}} \approx$

$2.1 \times 10^{45} \text{ erg s}^{-1}$ ). The Eddington ratio is therefore  $\lambda_{\text{Edd}} \equiv L_{\gamma, \text{tot}}/L_{\text{edd}} \approx 0.36$ , consistent with Das et al. (2024). The total photon luminosity is also in good agreement with the bolometric luminosity reported by Woo & Urry (2002). Furthermore, our modeled (2–10) keV luminosity ( $L_X \approx 6.8 \times 10^{43} \text{ erg s}^{-1}$ ) aligns with observational constraints (Marinucci et al. 2016). The energy budget is also partitioned into a magnetic and a proton component. We can define the non-thermal proton luminosity with the accretion luminosity or with the diffusive escape luminosity, so  $L_p \approx 4\pi R_{\text{cor}}^2 v \int \varepsilon_p (dN_p/d\varepsilon_p) d\varepsilon_p$  with  $v = R_{\text{cor}}/t_{\text{adv}}$  or  $v = R_{\text{cor}}/t_{\text{esc}}$  respectively. This results in  $L_p \approx 2.6 \times 10^{43} \text{ erg s}^{-1}$  or  $L_p \approx 4.8 \times 10^{43} \text{ erg s}^{-1}$  respectively. Either way, the derived proton power is consistent with previous estimates (Das et al. 2024) and remains safely below the bolometric luminosity. The accreting turbulent luminosity is  $L_{\delta B} = 1.2 \times 10^{43} \text{ erg s}^{-1}$ . Together, these results indicate that the proposed scenario is energetically robust. However, the solution is not unique, as illustrated by the parameter degeneracies shown in Figs. 4 & 5.

The spectrum shown in Fig. 2 corresponds to our set of fiducial parameters. We will examine its sensitivity to this choice of parameters in the following section. Here, we discuss how the overall spectral shape departs from other models proposed in the literature. First, this spectrum represents an average over a time-dependent evolution through the coronal volume, while other models generically evaluate the spectrum as the steady state solution to the transport equation. To better visualize this time evolution, we plot in Fig. 3 the time-dependent spectra of a proton population (top panel) injected at an initial time  $t = 0$  together with the corresponding secondary neutrino spectra (middle panel). For each, the thick black line shows the average spectrum representative of a stationary corona, i.e., on timescales  $t \gg t_{\text{adv}}, t_{\text{esc}}$ . Early on ( $t \lesssim 0.2t_{\text{adv}}$ ), the proton spectrum  $\varepsilon_p^2 dN_p/d\varepsilon_p$  grows in intensity and to larger energies due to acceleration. This is in agreement with the standard result  $dN_p/d\varepsilon_p \propto \varepsilon_p^{-1-t_{\text{acc}}/t_{\text{esc}}}$  in the absence of energy losses and backreaction on the turbulence (Fermi 1954), implying that for  $t_{\text{acc}} < t_{\text{esc}}$ , as is the case here (Fig. 1),  $\varepsilon_p^2 dN_p/d\varepsilon_p$  is an increasing function of  $\varepsilon_p$ . However, once the proton energy density comes close to the turbulent energy density, damping becomes effective and nonlinear backreaction becomes effective. This effect is visible in the plot of the turbulent energy power spectrum in the lower panel, which reveals damping. In agreement with Lemoine et al. (2024), the acceleration rate drops for low energy particles, while higher-energy particles keep gaining energy by interacting with larger-scale modes. The proton spectrum then levels out, shaping a proton spectrum with, approximately,  $dN_p/d\varepsilon_p \propto \varepsilon_p^{-2}$ . A clear signature of this effect is to produce a flat extension to the neutrino spectrum, below the peak energy at  $\sim \text{TeV}$  energies, that results from  $pp$  interactions. Models that do not include the backreaction of accelerated particles on the turbulence, or that assume  $\xi_p \lesssim 10^{-3}$  (see thereafter), rather produce a neutrino spectral shape with a pronounced peak at TeV energies.

In our framework, the physically relevant stationary spectrum for the whole corona is set by  $t = t_{\text{adv}}$ , since advection limits particle residence time in the corona. If acceleration could continue past  $t_{\text{adv}}$ , the spectrum would eventually reach a steady state regime corresponding to  $\partial_t \mathcal{N}_p \approx 0$  in Eq. (6), shown by the green to orange curves in Fig. 3. This occurs at times exceeding the diffusive escape and energy loss timescales, i.e. at  $t \gtrsim 5 t_{\text{adv}}$  (red curve). As discussed in the following section, such a steady state could be achieved within one  $t_{\text{adv}}$  with a faster acceleration rate, e.g., a larger  $v_A$ . This would produce a mild pile-up in the proton spectrum, as a result of the competition between accel-

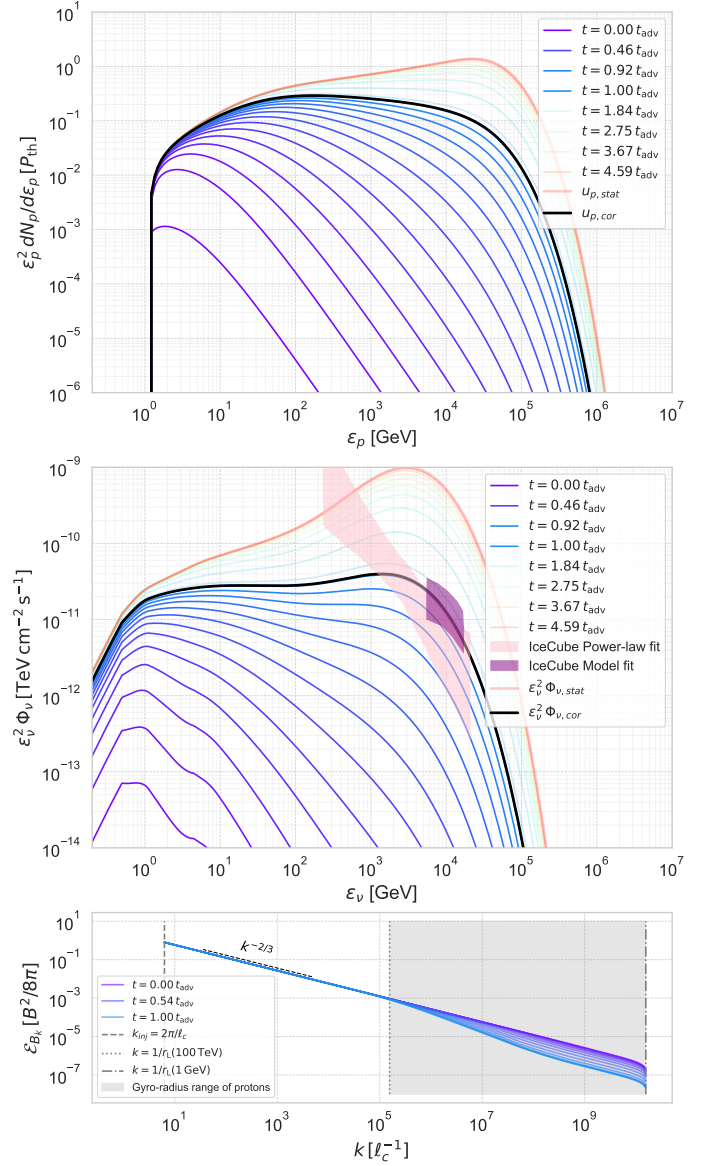


Fig. 3: Top panel: Time evolution of the integrated proton spectral energy distribution (SED) over the advection time  $t_{\text{adv}}$  (purple to blue), i.e. the plasma crossing time of the corona; the spectrum is expressed in units of the background plasma pressure. The stationary proton SED in the corona is shown in black. The green–orange curves display the proton SED evolution beyond  $t_{\text{adv}}$ . The red curve corresponds to the proton SED obtained by integrating up to times well in excess of  $t_{\text{adv}}$ , for illustration. These spectra correspond to the steady state solutions of Eq. (6). Middle panel: same as the top panel, for the neutrino flux. Bottom panel: Time evolution of the magnetic turbulent cascade during the advection time. The gray region highlights the part of the inertial range that dominates particle acceleration of protons up to 100 TeV.

eration and energy losses. This pile-up would be pronounced in the neutrino spectrum as a result of the strong dependence of  $pp$  losses on proton energy, see Fig. 3. The overall neutrino spectral shape would then display a characteristic pronounced peak at TeV energies, similar to those obtained in the literature not accounting for the feedback on turbulence (e.g., Yuan et al. 2026).

Such models can account for the observed neutrino spectrum at the price of tuning the proton injection fraction  $\xi_p$ , or the filling fraction of active regions in the corona, by the right amount. The dependency of the spectral shape on this parameter is now examined.

### 3.2. Exploration of parameter space

For given ambient physical conditions, the rates of energy loss are fixed, and hence the proton spectral shape is mostly governed by three parameters: the injection fraction  $\xi_p$  and the ratios of advection or escape to acceleration timescales (Sec. 2.3). We explore the influence of these various parameters in the present Section to assess the sensibility of the predicted neutrino spectral shapes on the choice of parameters.

Figure 4 shows the spectra for different non-thermal energy fractions,  $\xi_p$ . In order to obtain a meaningful comparison to observations, we slightly tune the Alfvénic velocity  $v_A$  to match the observed neutrino flux at a pivot point defined by  $E_\nu = 10$  TeV and (all-flavour) flux  $E_\nu^2 \Phi_\nu = 1.4 \times 10^{-11}$  erg/cm<sup>2</sup>s, see the corresponding figure. In practice, this implies increasing  $v_A$  as one decreases  $\xi_p$ ; other parameters remain fixed. One key observation is that, at low values of  $\xi_p$ , the neutrino spectrum becomes increasingly peaked. This occurs because turbulent damping is weak when  $\xi_p < 10^{-2}$ , implying that proton acceleration mostly takes place in the linear (or test-particle) regime. As noted earlier, the proton spectral shape then becomes hard, with approximately  $\varepsilon_p^2 dN_p/d\varepsilon_p \propto \varepsilon_p^{1-t_{\text{acc}}/t_{\text{esc}}}$ . In turn, this shape a steeper  $pp$  contribution to the neutrino flux.

At moderate values of the injection fraction and above,  $\xi_p \gtrsim 10^{-2}$ , proton acceleration becomes self-regulated by turbulent damping, and the proton spectrum converges toward a universal saturation state, whose total energy density is of the order of the total turbulent energy content. The model reliably reproduces the IceCube neutrino flux, independently of the precise value of  $\xi_p$ , shaping a neutrino spectral shape with a turn-over at energies below the peak ( $E_\nu \sim 3$  TeV here). The flat extension to lower energies is prominent for the largest value of  $\xi_p$ . As mentioned above, it is shaped by the  $pp$  contribution that follows the approximately flat proton spectrum.

We remark here that this contribution would be suppressed in proportion to  $n_p/n_e$  if pair loading becomes substantial (here,  $n_p/n_e = 1$ ). This scaling arises from the observation that the ratio  $n_p/n_e$  governs the plasma proton density, with  $n_e$  determined by the opacity constraint, yet it has little effect on the high-energy non-thermal proton content. The overall pressure of these protons indeed remains comparable to the turbulent magnetic pressure once turbulent damping becomes significant, see Eq. (13). Future high-sensitivity neutrino observations of NGC 1068 in this energy range could help discriminate between these possibilities.

We now turn to the influence of the ratio between the proton escape and acceleration timescales,  $t_{\text{esc}}/t_{\text{acc}}$  [Eq. (7)], while maintaining a constant ratio between the advection and acceleration timescales, whose influence is discussed thereafter. We satisfy these requirements by varying  $\ell_c$ , hence the ratio  $R_{\text{cor}}/\ell_c$  at constant  $R_{\text{cor}} = 15 r_g$ , together with  $v_A \propto (R_{\text{cor}}/\ell_c)^{-1/2}$ . Figure 5 illustrates the characteristic dependence of the various spectra on this ratio  $t_{\text{esc}}/t_{\text{acc}}$ . It confirms the anticipated result that  $t_{\text{esc}}/t_{\text{acc}} \gtrsim 1$  is a prerequisite to proton acceleration to high energies. In this limit, the proton spectrum acquires a near universal shape with approximately equal energy per decade, as above. This is a direct consequence of turbulence damping, which be-

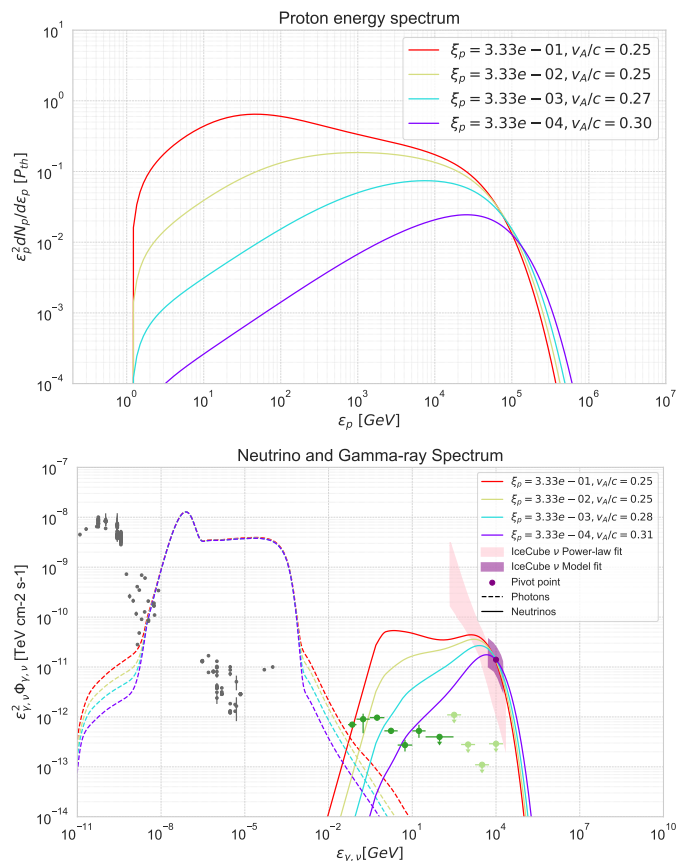


Fig. 4: Integrated proton (top panel), as well as photon and neutrino stationary (bottom panel) energy spectra. The initial energy fraction in non-thermal protons and the Alfvénic velocity are indicated for each model. The other parameters are  $L_d = 5.0 \times 10^{44}$  erg s<sup>-1</sup>,  $R_{\text{cor}} = 15 r_g$ ,  $\ell_c = 4.0 r_g$ ,  $v_{\text{adv}} = 0.03 c$ .

comes more prevalent when protons are strongly confined, as one would anticipate. As  $t_{\text{esc}}/t_{\text{acc}} \gtrsim 1$  takes larger values, the normalization of the proton spectrum rises due to more efficient confinement. However, this growth is ultimately limited by the finite turbulent energy reservoir, leading to a saturation of the proton energy density at large values of  $t_{\text{esc}}/t_{\text{acc}}$ . The corresponding neutrino spectra also exhibits the universal shape when the turbulence feedback is significant, and naturally reproduce the observed neutrino spectrum for  $t_{\text{esc}}/t_{\text{acc}} > 1$ .

To gauge the influence of varying  $t_{\text{adv}}/t_{\text{acc}}$  while maintaining  $t_{\text{esc}}/t_{\text{acc}}$  fixed, we now vary  $v_{\text{adv}}$  with all others parameters fixed to their value in Sect. 3.1. We recall that the value chosen so far,  $v_{\text{adv}} = 0.03 c$ , corresponds to the standard radial inflow velocity at a position  $R_{\text{cor}} = 15 r_g$ . Varying this parameter thus offers a way of exploring different corona scenarios, just as it tests our assumption of spatially uniform  $v_{\text{adv}}$ . As expected, increasing  $t_{\text{adv}}/t_{\text{acc}}$  shifts the energy cutoff toward higher values (see Fig. 6). This is because the advection timescale  $t_{\text{adv}}$  sets the duration over which protons are accelerated and therefore determines the maximum achievable energy. In the diffusive regime, neglecting escape and radiative losses, the mean proton momentum evolves as  $\langle p \rangle_{t=t_{\text{adv}}} = \langle p \rangle_{t=0} \exp(4t_{\text{adv}}/t_{\text{acc}})$ . Thus, for the stationary proton population to reach the characteristic energies  $E \sim 10 - 100$  TeV required to reproduce the observed neutrino flux,  $t_{\text{adv}}/t_{\text{acc}}$  must be of order a few. However, for large values of  $t_{\text{adv}}/t_{\text{acc}}$ , the cutoff energies converge between 10 and 100 TeV.

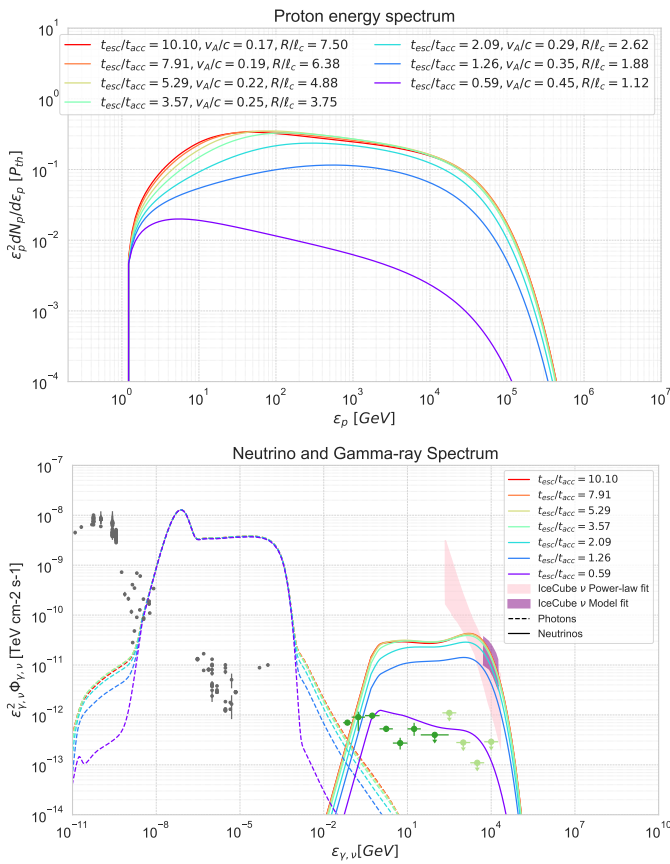


Fig. 5: Proton, photon, and neutrino stationary spectra for different coronal microphysics parameters, characterized by varying dimensionless time ratios  $t_{esc}/t_{acc}$ . The parameters  $v_A$  and  $\ell_c$  are varied, while the others are fixed to  $L_d = 5.0 \times 10^{44} \text{ erg s}^{-1}$ ,  $R_{cor} = 15 r_g$ ,  $\xi_p = 0.1$ , and  $v_{adv} = 0.03 c$ . The same color in both panels corresponds to the same parameter set.

This behaviour arises because, once protons reach the energy at which photohadronic ( $p\gamma$ ) losses dominate over acceleration, the losses timescale, rather than the advection timescale, determine the cutoff. In the limit of large  $t_{adv}/t_{acc}$ , the stationary spectrum asymptotically approaches the solution obtained when advective proton losses are neglected, corresponding to the red curve in Fig. 3. For  $v_{adv} < 0.02 c$  the multi-messenger flux exceeds the IceCube bound and the  $\gamma$ -ray constraints, unless  $\xi_p$  is artificially reduced to low values. A clear measurement of the neutrino spectrum in the corresponding range could potentially disentangle the various possibilities and thus shed light on the inner physics of the corona.

Finally, let us briefly address the influence of the microphysical transport model on the neutrino spectral shape. Our parameter study has thus far relied on the standard diffusive Fokker-Planck framework, with parameters derived from numerical kinetic simulations. However, exploring the alternative models outlined in Sec. 2.2 reveals that the neutrino spectral shape remains relatively unaffected by this choice in the self-regulated regime. This insensitivity arises because the proton spectrum adopts a nearly universal, flat shape under these conditions. This is demonstrated in Appendix A, Fig. A.1.

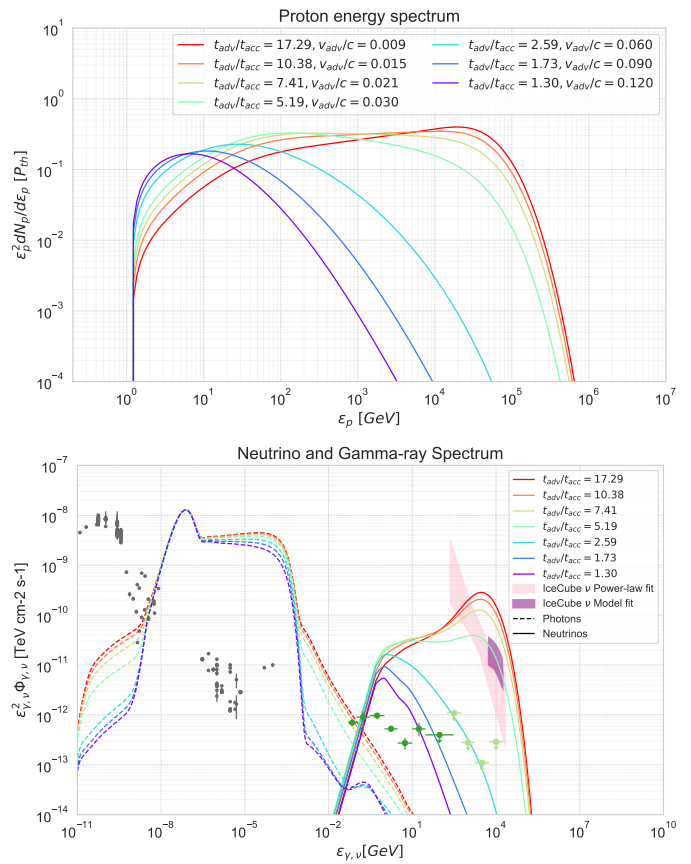


Fig. 6: Same as Fig. 5 but for different time ratios  $t_{adv}/t_{acc}$ .  $v_{adv}$  is varied. The other parameters are  $L_d = 5.0 \times 10^{44} \text{ erg s}^{-1}$ ,  $R_{cor} = 15 r_g$ ,  $\xi_p = 0.1$ ,  $v_A = 0.25 c$ ,  $\ell_c = 4.0 r_g$ .

### 3.3. A template neutrino average spectrum

This exploration of parameter space reveals that the proton and neutrino energy spectra take different shapes depending on the ratios  $t_{adv}/t_{acc}$  and  $t_{esc}/t_{acc}$ . The injected proton fraction  $\xi_p$  does not strongly influence the spectral shape provided  $\xi_p \gtrsim 10^{-2}$ . In a situation such as the present one, where the spectral shape varies substantially as a function of one or two parameters whose actual values cannot take precisely uniform values through the corona, or precisely constant ones in time, the actual spectral shape is bound to represent an average of the various possibilities. We thus explore here the possibility of an extended distribution of these parameters. This extended distribution can be understood in various ways. For instance, the physical conditions can vary on timescales larger than  $t_{adv}$ , implying that the observed neutrino spectrum is effectively a time average. Or, the corona itself can comprise patchy regions of small extent that each contribute to energization with local conditions.

We simplify the problem by assuming that the magnetization  $\sigma_{\delta B}$ , which controls the acceleration rate [Eq. (8)], is the only parameter subject to spatial fluctuations. We model it as a random variable with a prescribed distribution  $w(\sigma)$ , normalized such that the mean value  $\langle \sigma \rangle = \int d\sigma \sigma w(\sigma)$  is fixed to 0.04 (corresponding to  $v_A \simeq 0.2 c$ ), consistent with the coronal conditions discussed in Sec. 2.1. For illustration, we consider both a Gaussian distribution and a power-law distribution of weights,  $w(\sigma) \propto \sigma^{-k}$  with  $k = 2$ , over the interval  $\sigma \in [0.01, 2]$  (see e.g. Grosej et al. 2026). In practice we compute neutrino spectra as in Sect. 3.1, but for different magnetizations. We then average

the neutrino spectra according to the prescription in  $w(\sigma)$ . The resulting (averaged) neutrino spectra are shown in Fig. 7. We adopt a non-thermal proton fraction  $\xi_p = 0.1$ , in line with our fiducial value, for which the non-thermal proton energy density takes values of the order of the turbulent energy density and does not strongly affect the spectral shape. We find that the average spectral shape is insensitive to the choice of weight distribution. The resulting neutrino spectrum exhibits the characteristic “universal” profile: a broad peak with a low-energy extension dominated by  $pp$  interactions, tracing the underlying proton density. As discussed above, this component could be suppressed in the presence of significant pair loading in the corona. At higher energies, the spectrum extends beyond the peak compared to the fiducial single-zone model (Fig. 2), reflecting the contribution of intermittent (in space or time) regions with locally enhanced acceleration efficiency. Nevertheless, the averaged spectrum still displays a pronounced cutoff at a few tens of TeV, set by photohadronic losses. This indicates that, within the present framework, it remains challenging to account for neutrino emission extending beyond  $\sim 100$  TeV.

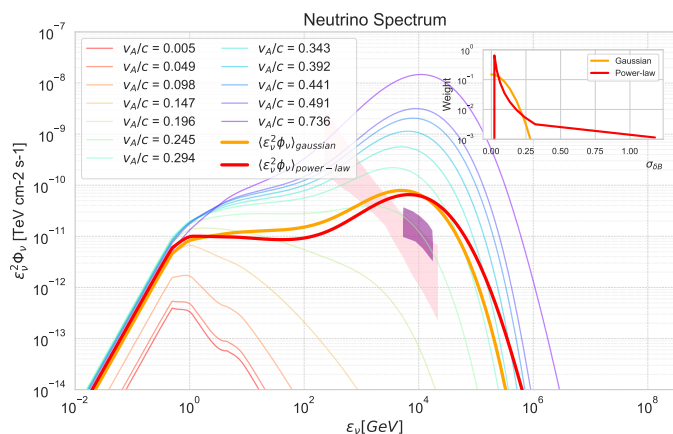


Fig. 7: Neutrino spectra obtained by averaging over different realizations of the coronal magnetization  $\sigma_{\delta B}$ , treated as a random variable controlling the acceleration rate. Two weighting schemes are shown: a Gaussian distribution and a power-law distribution  $w(\sigma) \propto \sigma^{-2}$ , both normalized to the same mean magnetization  $\langle \sigma \rangle = 0.04$ .

### 3.4. Extension to other Seyfert galaxies

A natural extension of this work is to explore how our model applies to other X-ray–bright Seyfert galaxies. Recent IceCube observations (Abbasi et al. 2026) suggest a possible trend in the  $(F_{\nu}, E_{\nu})$  plane: sources detected at higher characteristic neutrino energies tend to exhibit lower fluxes (see Fig. 8), with the notable exception of CGCG 420–015. Such a trend could potentially result from a varying X-ray luminosity (Yang et al. 2026). An increase in coronal luminosity enhances the density of target photons (if the size of the corona does not vary), thereby boosting the efficiency of  $py$  interactions. This leads to a higher neutrino flux, but also to stronger photohadronic cooling, which shifts the proton cutoff, and consequently the neutrino cutoff, to lower energies. Conversely, lower luminosities reduce the neutrino flux while allowing protons to reach higher maximum energies, shifting the neutrino emission toward higher energies. This mechanism can therefore account for part of the observed diversity in the neutrino properties of Seyfert galaxies.

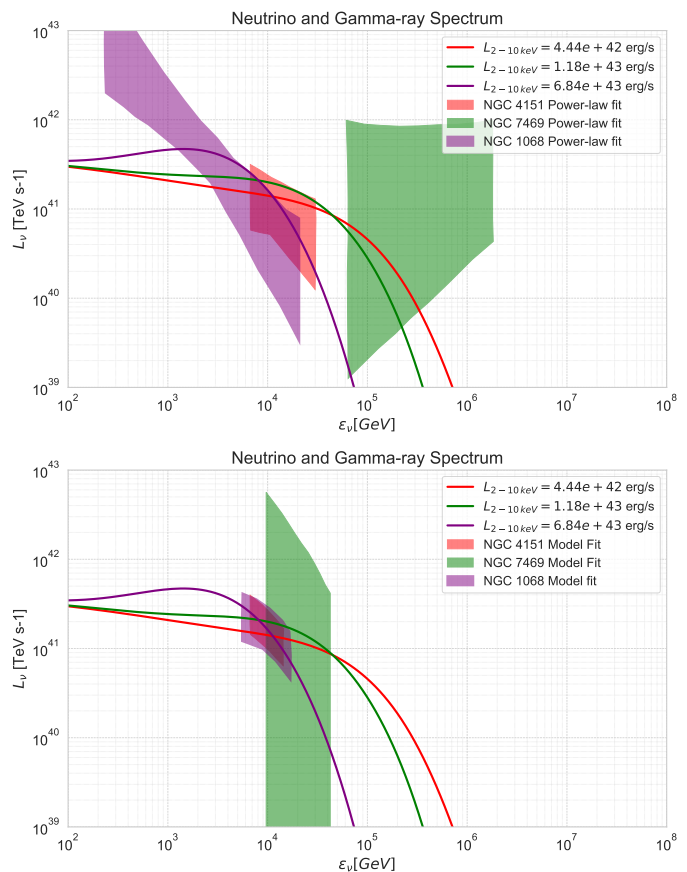


Fig. 8: Predicted stationary neutrino spectra for different Seyfert galaxies, compared with IceCube inferred fluxes. *Top panel*: comparison with IceCube results obtained under a power-law assumption. *Bottom panel*: comparison with IceCube results inferred using a disk–corona model. In both panels, model predictions are computed using the same fiducial parameters as in Sec. 3.1, with variations in the disk luminosity.

Figure 8 compares the neutrino luminosities inferred by IceCube for NGC 1068, NGC 4151, and NGC 7469 (under a power-law assumption or a disk–corona model assumption), with the predictions of our model. Starting from the fiducial parameter set described in Sec. 3.1, we vary only the disk luminosity (and thus the coronal X-ray luminosity) to match the observed 2 – 10 keV luminosities of NGC 4151 ( $L_{2-10\text{ keV}} = 5_{-2}^{+3} \times 10^{42}$  erg s<sup>-1</sup>; Kumar et al. 2024) and NGC 7469 ( $L_{2-10\text{ keV}} = (1.0 - 1.7) \times 10^{43}$  erg s<sup>-1</sup>; Prince et al. 2025). Despite its simplicity, this approach reproduces the neutrino emission levels of these Seyfert galaxies reasonably well. In particular, it accommodates, within the relatively large error bars, the potential  $\sim 100$  TeV neutrino detection that could be associated with NGC 7469, highlighting the ability of the model to capture the broad range of observed neutrino energies.

## 4. Conclusions

In this paper, we have presented a self-consistent numerical framework to model high-energy neutrino production in radiatively dense environments, and we have applied it to the case of NGC 1068 to derive state-of-the-art predictions for the neutrino spectrum in the TeV range. This numerical framework leverages the implementation of hadronic and radiative loss channels and

the self-consistent treatment of electromagnetic cascades in the numerical tool AM3 (Klinger et al. 2024). With respect to AM3, a new and noteworthy feature is to offer a self-consistent time-dependent model of stochastic acceleration for the protons, properly including the backreaction of proton acceleration on the turbulent cascade (and hence on the acceleration itself), and incorporating detailed prescriptions from microphysics. One advantage of this approach is to provide a unified description of particle acceleration and multi-messenger emission in environments that are possibly radiatively dense, as is the case for hidden neutrino sources. Here we have held fixed the electron distribution function, as they evolve on short timescales compared to those of protons in the case investigated, but future studies should incorporate detailed energy loss and energization processes for mildly relativistic electrons, as in existing models of X-ray emission from black hole coronae, to improve self-consistency.

We have used this numerical framework to examine the case of NGC 1068 as a high-energy neutrino source in Sec. 3. We have thus demonstrated that the observed neutrino spectrum of NGC 1068 can be satisfactorily reproduced using physically motivated, standard parameters. In particular, a coronal size  $R_{\text{cor}} \sim 5 - 20 r_g$ , an Alfvén velocity  $v_A = O(0.2c)$ , a coherence length  $\ell_c \sim R_{\text{cor}}/4$ , and an advection velocity  $v_{\text{adv}} = O(0.03c)$  yield acceleration, escape, and advection timescales satisfying  $t_{\text{acc}} \lesssim t_{\text{esc}}, t_{\text{adv}}$ , allowing protons to reach the required energies. The inferred magnetic field strength,  $\delta B = O(10^3)G$ , assuming near-equipartition, and a proton-to-lepton ratio  $n_p/n_e \lesssim 1$  are consistent with standard coronal models. The resulting neutrino emission is compatible with current  $\gamma$ -ray constraints, in agreement with previous studies (Eichmann et al. 2022; Fang et al. 2023; Das et al. 2024; Yuan et al. 2026).

For the given set of parameters, the coupled evolution of proton acceleration and turbulence establishes a natural self-regulating mechanism. The accelerated protons, through turbulent damping, extract energy from the cascade, thereby curbing their own growth and maintaining the non-thermal proton energy density at a level comparable to that of the turbulent energy density. This self-regulation provides a natural explanation for the normalization of the neutrino flux observed from NGC 1068.

We have also demonstrated that this model successfully reproduces the IceCube data, within the relatively large error bars, for the Seyfert galaxies NGC 4151 and NGC 7469, using identical parameters except for their X-ray luminosity, which was adjusted to match observed values.

Our exploration of the parameter space has also allowed us to extract a generic template for the neutrino spectrum: a gradual rise to a peak around  $\sim 1 - 10$  TeV, followed by a decline with an approximately power-law-like behavior over a limited energy range. This high-energy suppression directly reflects the cutoff in the proton distribution due to efficient photohadronic losses. Notably, the nearly flat extension below the peak, shaped by  $pp$  interactions, serves as a useful indicator of the proton density in the corona and, consequently, the pair-loading factor.

Overall, the interplay between magnetic turbulence and radiative processes in the corona sets both the normalization and the shape of the neutrino emission. In this sense, neutrino observations already provide a direct probe of coronal plasma conditions, despite existing parameter degeneracies.

*Acknowledgements.* The authors are grateful to D. Grosej for insightful discussions. This work was supported by the French Agence Nationale de la Recherche, ANR, project ANR-25-CE31-3279.

## References

- Aartsen, M. G., Ackermann, M., Adams, J., et al. 2020, *Phys. Rev. Lett.*, 124, 051103
- Abbasi, R., Ackermann, M., Adams, J., et al. 2026, *Astrophys. J. Lett.*, 1000, L26
- Abbasi, R., Ackermann, M., Adams, J., et al. 2025a, *Astrophys. J.*, 981, 131
- Abbasi, R., Ackermann, M., Adams, J., et al. 2025b, *Astrophys. J.*, 988, 141
- Ajello, M., Murase, K., & McDaniel, A. 2023, *Astrophys. J. Lett.*, 954, L49
- Ambrosone, A. 2024, *J. Cosmol. Astropart. Phys.*, 2024, 075
- Belmont, R., Malzac, J., & Marcowith, A. 2008, *Astron. Astrophys.*, 491, 617
- Beloborodov, A. M. 2017, *Astrophys. J.*, 850, 141
- Berezinskii, V. S., Bulanov, S. V., Dogiel, V. A., & Ptuskin, V. S. 1990, *Astron. Nachr. North-Holland, Amsterdam*, 312, 413
- Bresci, V., Lemoine, M., Gremillet, L., et al. 2022, *Phys. Rev. D*, 106, 023028
- Cerruti, M., Rudolph, A., Petropoulou, M., et al. 2026, *Astrophys. J. Suppl. Ser.*, 282, 22
- Chang, Y.-L., Brandt, C. H., & Giommi, P. 2020, *Astron. Comput.*, 30, 100350
- Comisso, L. & Sironi, L. 2019, *Astrophys. J.*, 886, 122
- Comisso, L. & Sironi, L. 2022, *Astrophys. J. Lett.*, 936, L27
- Coppi, P. S. 1992, *Mon. Not. R. Astron. Soc.*, 258, 657
- Das, A., Zhang, B. T., & Murase, K. 2024, *Astrophys. J.*, 972, 44
- Das, S., Xu, S., & Nättilä, J. 2025, arXiv e-prints, arXiv:2506.04212
- Demidem, C., Lemoine, M., & Casse, F. 2020, *Phys. Rev. D*, 102, 023003
- Dmytriiev, A., van der Merwe, F., & Böttcher, M. 2026, arXiv e-prints, arXiv:2603.09394
- Dovčiak, M., Papadakis, I. E., Kammoun, E. S., & Zhang, W. 2022, *Astron. Astrophys.*, 661, A135
- Eichmann, B., Oikonomou, F., Salvatore, S., Dettmar, R.-J., & Tjus, J. B. 2022, *Astrophys. J.*, 939, 43
- Fabian, A. C., Lohfink, A., Belmont, R., Malzac, J., & Coppi, P. 2017, *Mon. Not. R. Astron. Soc.*, 467, 2566
- Fabian, A. C., Lohfink, A., Kara, E., et al. 2015, *Mon. Not. R. Astron. Soc.*, 451, 4375
- Fang, K., Rodriguez, E. L., Halzen, F., & Gallagher, J. S. 2023, *Astrophys. J.*, 956, 8
- Fermi, E. 1954, *Astrophys. J.*, 119, 1
- Fiorillo, D. F. G., Comisso, L., Peretti, E., Petropoulou, M., & Sironi, L. 2024a, *Astrophys. J.*, 974, 75
- Fiorillo, D. F. G., Comisso, L., Peretti, E., Petropoulou, M., & Sironi, L. 2025, *Astrophys. J.*, 989, 215
- Fiorillo, D. F. G., Petropoulou, M., Comisso, L., Peretti, E., & Sironi, L. 2024b, *Astrophys. J. Lett.*, 961, L14
- Frank, J., King, A., & Raine, D. J. 2002, *Accretion Power in Astrophysics*, 398
- Galeev, A. A., Rosner, R., & Vaiana, G. S. 1979, *Astrophys. J.*, 229, 318
- Ghisellini, G. & Tavecchio, F. 2009, *Mon Not R Astron Soc*, 397, 985
- Gong, X.-W., Liu, R.-Y., Zhang, Z.-L., Asano, K., & Lemoine, M. 2025, *Astrophys. J.*, 989, 99
- Gorunov, E. A., Grošelj, D., & Bacchini, F. 2025, *Phys. Rev. Lett.*, 135, 065201
- Grošelj, D., Hakobyan, H., Beloborodov, A. M., Sironi, L., & Philippov, A. 2024, *Phys. Rev. Lett.*, 132, 085202
- Grošelj, D., Philippov, A., Beloborodov, A. M., & Mushotzky, R. 2026, arXiv e-prints, arXiv:2601.00518
- Herrera, G. 2025, *Phys. Dark Univ.*, 50, 102156
- Hinkle, J. T. & Mushotzky, R. 2021, *Mon. Not. R. Astron. Soc.*, 506, 4960
- IceCube, T., Fermi-LAT, MAGIC, et al. 2018, *Science*, 361, eaat1378
- IceCube Collaboration, Aartsen, M. G., Ackermann, M., et al. 2018, *Science*, 361, 147
- IceCube Collaboration, Abbasi, R., M. Ackermann, et al. 2022, *Science*, 378, 538
- Inoue, Y., Khangulyan, D., Inoue, S., & Doi, A. 2019, *Astrophys. J.*, 880, 40
- Jaffe, W., Meisenheimer, K., Röttgering, H. J. A., et al. 2004, *Nature*, 429, 47
- Kakuwa, J. 2016, *Astrophys. J.*, 816, 24
- Kammoun, E., Lohfink, A. M., Masterson, M., et al. 2024, *Front. Astron. Space Sci.*, 10, 1308056
- Kantzas, D., Markoff, S., Cooper, A. J., et al. 2023, *Mon. Not. R. Astron. Soc.*, 524, 1326
- Karavola, D., Petropoulou, M., Fiorillo, D. F. G., Comisso, L., & Sironi, L. 2025, *J. Cosmol. Astropart. Phys.*, 2025, 075
- Kempski, P., Fielding, D. B., Quataert, E., et al. 2023, *Mon. Not. R. Astron. Soc.*, 525, 4985
- Kheirandish, A., Murase, K., & Kimura, S. S. 2021, *Astrophys. J.*, 922, 45
- Kimura, S. S., Tomida, K., & Murase, K. 2019, *Mon. Not. R. Astron. Soc.*, 485, 163
- Klinger, M., Rudolph, A., Rodrigues, X., et al. 2024, *Astrophys. J. Suppl. Ser.*, 275, 4
- Kumar, S., Dewangan, G. C., Gandhi, P., et al. 2024, *Astrophys. J.*, 975, 73
- Lemoine, M. 2019, *Phys. Rev. D*, 99, 083006
- Lemoine, M. 2021, *Phys. Rev. D*, 104, 063020
- Lemoine, M. 2022, *Phys. Rev. Lett.*, 129, 215101

- Lemoine, M. 2023, *J. Plasma Phys.*, 89, 175890501
- Lemoine, M. 2025, *Phys. Rev. E*, 112, 015205
- Lemoine, M. & Malkov, M. A. 2020, *Mon. Not. R. Astron. Soc.*, 499, 4972
- Lemoine, M., Murase, K., & Rieger, F. 2024, *Phys. Rev. D*, 109, 063006
- Lemoine, M. & Rieger, F. 2025, *Astron. Astrophys.*, 697, A124
- Lianou, S., Barmby, P., Mosenkov, A. A., Lehnert, M., & Karczewski, O. 2019, *Astron. Astrophys.*, 631, A38
- Lopez-Rodriguez, E., Fuller, L., Alonso-Herrero, A., et al. 2018, *Astrophys. J.*, 859, 99
- Lu, M.-X., Liang, Y.-F., Wang, X.-G., & Ouyang, X.-R. 2025, arXiv e-prints, arXiv:2503.09426
- Lynn, J. W., Quataert, E., Chandran, B. D. G., & Parrish, I. J. 2014, *Astrophys. J.*, 791, 71
- MAGIC Collaboration, Acciari, V. A., Ansoldi, S., et al. 2019, *Astrophys. J.*, 883, 135
- Marinucci, A., Bianchi, S., Matt, G., et al. 2016, *Mon. Not. R. Astron. Soc.*, 456, L94
- Mbarek, R., Philippov, A., Chernoglazov, A., Levinson, A., & Mushotzky, R. 2024, *Phys. Rev. D*, 109, L101306
- Meringolo, C., Cruz-Osorio, A., Rezzolla, L., & Servidio, S. 2023, *Astrophys. J.*, 944, 122
- Murase, K. 2022, *Astrophys. J. Lett.*, 941, L17
- Murase, K., Karwin, C. M., Kimura, S. S., Ajello, M., & Buson, S. 2024, *Astrophys. J. Lett.*, 961, L34
- Murase, K., Kimura, S. S., & Mészáros, P. 2020, *Phys. Rev. Lett.*, 125, 011101
- Murase, K., Kimura, S. S., Mukhopadhyay, M., & Bhattacharya, M. 2026, arXiv e-prints, arXiv:2602.20145
- Nättilä, J. 2024, *Nature Comm.*, 15, 7026
- Neronov, A., Savchenko, D., & Semikoz, D. V. 2024, *Phys. Rev. Lett.*, 132, 101002
- Nhat Ly, M., Inoue, Y., Sentoku, Y., & Sano, T. 2026, arXiv e-prints, arXiv:2601.01999
- Padovani, P., Resconi, E., Ajello, M., et al. 2024, *Nat. Astron.*, 8, 1077
- Pezzi, O., Blasi, P., & Matthaeus, W. H. 2022, *Astrophys. J.*, 928, 25
- Poutanen, J. & Svensson, R. 1996, *Astrophys. J.*, 470, 249
- Prince, R., Hernández Santisteban, J. V., Horne, K., et al. 2025, *Mon. Not. R. Astron. Soc.*, 541, 642
- Pugliese, F., Brodiano, M., Andrés, N., & Dmitruk, P. 2023, *Astrophys. J.*, 959, 28
- Reusch, S., Stein, R., Kowalski, M., et al. 2022, *Phys. Rev. Lett.*, 128
- Ricci, C., Ho, L. C., Fabian, A. C., et al. 2018, *Mon. Not. R. Astron. Soc.*, 480, 1819
- Rodrigues, X., Paliya, V. S., Garrappa, S., et al. 2024, *Astron. Astrophys.*, 681, A119
- Rybicki, G. B. & Lightman, A. P. 1979, A Wiley-Interscience Publication
- Schlickeiser, R. 2002, *Cosmic Ray Astrophysics* (Springer, Berlin)
- Sciaccaluga, A. & Tavecchio, F. 2022, *Mon. Not. R. Astron. Soc.*, 517, 2502
- Shakura, N. I. & Sunyaev, R. A. 1973, *Astron. Astrophys.*, 24, 337
- Sioulas, N., Isliker, H., & Vlahos, L. 2020a, *Astrophys. J. Lett.*, 895, L14
- Sioulas, N., Isliker, H., Vlahos, L., Koumtzis, A., & Pisokas, T. 2020b, *Mon. Not. R. Astron. Soc.*, 491, 3860
- Sironi, L. & Beloborodov, A. M. 2020, *Astrophys. J.*, 899, 52
- Sridhar, N., Ripperda, B., Sironi, L., Davelaar, J., & Beloborodov, A. M. 2025, *Astrophys. J.*, 979, 199
- Stein, R., Velzen, S. v., Kowalski, M., et al. 2021, *Nat. Astron.*, 5, 510–518
- Stern, B. E., Poutanen, J., Svensson, R., Sikora, M., & Begelman, M. C. 1995, *Astrophys. J. Lett.*, 449, L13
- Testagrossa, F., Fiorillo, D. F. G., Comisso, L., et al. 2026, arXiv e-prints, arXiv:2603.18214
- The Fermi Collaboration. 2020, *Astrophys. J. Suppl. Ser.*, 247, 33
- Trotta, D., Franci, L., Burgess, D., & Hellinger, P. 2020, *Astrophys. J.*, 894, 136
- Tully, R. B., Rizzi, L., Shaya, E. J., et al. 2009, *Astron. J.*, 138, 323
- Veledina, A., Vurm, I., & Poutanen, J. 2011, *Mon. Not. R. Astron. Soc.*, 414, 3330
- Wong, K., Zhdankin, V., Uzdensky, D. A., Werner, G. R., & Begelman, M. C. 2020, *Astrophys. J. Lett.*, 893, L7
- Wong, K. W., Zhdankin, V., Uzdensky, D. A., Werner, G. R., & Begelman, M. C. 2025, *Mon. Not. R. Astron. Soc.*, 543, 1842
- Woo, J. & Urry, C. M. 2002, *Astrophys. J.*, 579, 530–544
- Xu, S. & Lazarian, A. 2022, *Astrophys. J.*, 942, 21
- Yang, Q.-R., Chen, X.-B., Liu, R.-Y., Wang, X.-Y., & Lemoine, M. 2025, *Astrophys. J.*, 995, 166
- Yang, Q.-R., Liu, R.-Y., & Wang, X.-Y. 2026, arXiv e-prints, arXiv:2602.20969
- Yuan, C., Fiorillo, D. F. G., Petropoulou, M., & Liu, Q. 2026, *Phys. Rev. D*, 113, 043016
- Yuan, C., Winter, W., & Lunardini, C. 2024, *Astrophys. J.*, 969, 136
- Zdziarski, A. A. 1985, *Astrophys. J.*, 289, 514
- Zdziarski, A. A. & Lightman, A. P. 1985, *Astrophys. J. Lett.*, 294, L79
- Zhdankin, V., Werner, G. R., Uzdensky, D. A., & Begelman, M. C. 2017, *Phys. Rev. Lett.*, 118, 055103

## Appendix A: Proton, photon and neutrino spectra for different acceleration schemes

In this Appendix, we present a comparative exploration of the impact of different acceleration schemes on the resulting particle spectra.

In Fig. A.1, we compare several prescriptions used to model stochastic particle acceleration (see Sec. 2.2): the Fokker–Planck (diffusive) scheme, the generalized Fermi approach, and a first-order (“Fermi I”) scheme. In the latter case, stochastic acceleration is replaced by a systematic drift in momentum space. This contribution is described by an advective term in momentum space,

$$\mathcal{L}_{\text{Adv}} \mathcal{N}_p \equiv -\partial_p (A_p \mathcal{N}_p), \quad (\text{A.1})$$

where  $A_p$  is an effective momentum drift coefficient. The corresponding acceleration rate is defined as  $v_{\text{acc}} \equiv A_p/p$ . Although the exact momentum dependence of  $A_p$  is uncertain, we adopt here a constant acceleration rate,

$$v_{\text{acc}} \simeq \frac{4v_A^2}{3\ell_c c},$$

chosen such that the systematic acceleration operates with an efficiency comparable to that of diffusive stochastic acceleration.

These schemes are evaluated for the same set of physical parameters in order to isolate the role of the microphysics. We find that their impact on the resulting proton and neutrino spectra remains limited, provided that the injected non-thermal proton energy fraction is sufficiently large. In this regime, the system enters a feedback-dominated state in which the proton population self-regulates through its interaction with the turbulent cascade.

As a result, the various acceleration prescriptions lead to qualitatively similar spectra: the proton spectral energy density saturates at a level comparable to the thermal plasma pressure, and exhibits a high-energy cutoff at a few tens of TeV due to efficient photohadronic losses. The associated neutrino spectra inherit these features.

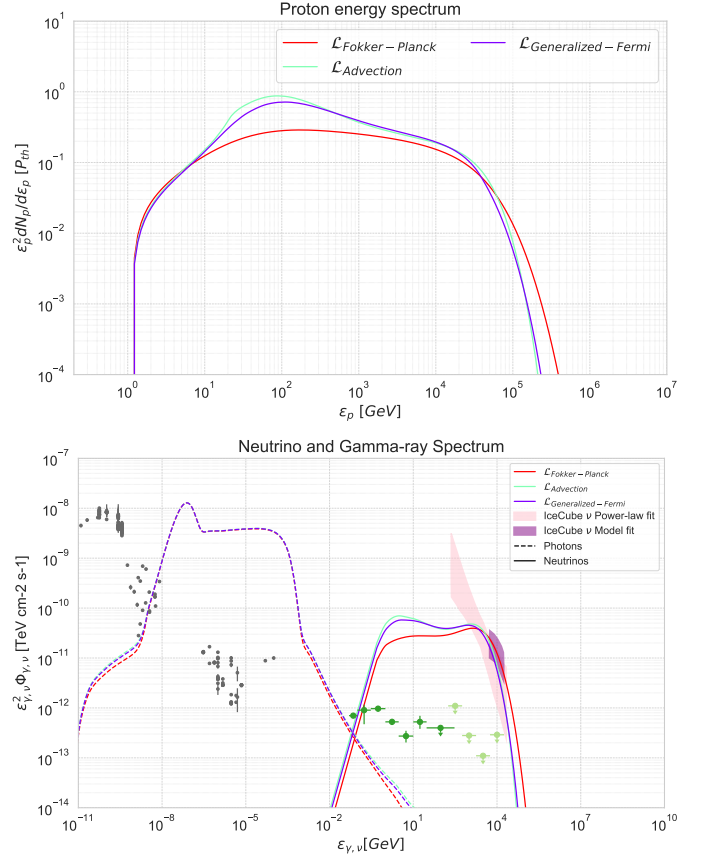


Fig. A.1: Proton, photon and neutrino stationary spectra with different microphysics description of the proton acceleration. For every acceleration scheme, the same parameters are used.  $L_d = 5.0 \times 10^{44} \text{ erg s}^{-1}$ ,  $R_{\text{cor}} = 15 r_g$ ,  $\xi_p = 0.1$ ,  $\ell_c = 4.0 r_g$ ,  $v_{\text{adv}} = 0.03 c$ ,  $v_A = 0.25 c$ .